NeuroImage xxx (2009) xxx–xxx

Contents lists available at ScienceDirect

NeuroImage

journal homepage: www.elsevier.com/locate/ynimg

Technical Note

Ultrahigh-frequency EEG during fMRI: Pushing the limits of imaging-artifact correction

Frank Freyer [a,c,*], Robert Becker [a,c], Kimitaka Anami [b], Gabriel Curio [a,c], Arno Villringer [a,c,d,e], Petra Ritter [a,c,e]

[a] Berlin NeuroImaging Center and Department of Neurology, Charité Universitaetsmedizin, Charitéplatz 1, 10117 Berlin, Germany
[b] Musashino Mental Hospital, Saitama, Japan
[c] Bernstein Center for Computational Neuroscience, Berlin, Germany
[d] Max Planck Institute for Brain and Cognitive Sciences, Leipzig, Germany
[e] Berlin School of Mind and Brain & Mind and Brain Institute, Philosophical Institute Humboldt University Berlin, Germany

ARTICLE INFO

Article history:
Received 25 November 2008
Revised 13 May 2009
Accepted 8 June 2009
Available online xxxx

ABSTRACT

Although solutions for imaging-artifact correction in simultaneous EEG–fMRI are improving, residual artifacts after correction still considerably affect the EEG spectrum in the ultrafast frequency band above 100 Hz. Yet this band contains subtle but valuable physiological signatures such as fast gamma oscillations or evoked high-frequency (600 Hz) bursts related to spiking of thalamocortical and cortical neurons. Here we introduce a simultaneous EEG–fMRI approach that integrates hard and software modifications for continuous acquisition of ultrafast EEG oscillations during fMRI. Our approach is based upon and extends the established method of averaged artifact subtraction (AAS). Particularly for recovery of ultrahigh-frequency EEG signatures, AAS requires invariantly sampled and constant imaging-artifact waveforms to achieve optimal imaging-artifact correction. Consequently, we adjusted our acquisition setup such that both physiological ultrahigh-frequency EEG and invariantly sampled imaging artifacts were captured. In addition, we extended the AAS algorithm to cope with other, non-sampling related sources of imaging-artifact variations such as subject movements. A cascaded principal component analysis finally removed remaining imaging-artifact residuals. We provide a detailed evaluation of averaged ultrahigh-frequency signals and unaveraged broadband EEG spectra up to 1 kHz. Evoked nanovolt-sized high-frequency bursts were successfully recovered during periods of MR data acquisition afflicted by imaging artifacts in the millivolt range. Compared to periods without imaging artifacts they exhibited the same mean amplitudes, latencies and waveforms and a signal-to-noise ratio of 72%. Furthermore we identified consistent dipole sources. In conclusion, ultrafast EEG oscillations can be continuously monitored during fMRI using the proposed approach.

© 2009 Elsevier Inc. All rights reserved.

Introduction

Simultaneous acquisition of electroencephalography (EEG) and functional magnetic resonance imaging (fMRI) aims at combining the strength of both methods and investigating spontaneous and event-related brain activity with high temporal and spatial precision. However, MR-related artifacts that are induced in the EEG constitute a serious challenge (Laufs et al., 2008; Ritter and Villringer, 2006; Salek-Haddadi et al., 2003). Appropriate removal of those artifacts is essential for the recovery of the true underlying neuronal signal and various methods have been developed for that purpose. The importance of a thorough evaluation of these methods with respect to artifact removal and deterioration of the underlying signal has been demonstrated (Grouiller et al., 2007; Ritter et al., 2007). Numerous types of EEG signatures obtained during fMRI have been investigated so far, e.g. epileptiform activity (Benar et al., 2006; Hamandi et al., 2008; Krakow et al., 2001; Lemieux et al., 2001; Salek-Haddadi et al., 2002), single-trial error-related negativity (Debener et al., 2005), cortical oscillations such as delta (Czisch et al., 2004; Dang-Vu et al., 2008), theta (Sammer et al., 2007; Scheeringa et al., 2008), alpha (de Munck et al., 2007; Goldman et al., 2002; Goncalves et al., 2006; Laufs et al., 2003a; Martinez-Montes et al., 2004; Moosmann et al., 2003), rolandic/mu (Ritter et al., 2008c), or beta (Laufs et al., 2003b) rhythms, as well as somatosensory- (Iannetti et al., 2005; Schubert et al., 2008), auditory- (Benar et al., 2007; Eichele et al., 2005; Liebenthal et al., 2003), and visually-evoked potentials (Becker et al., 2005;

Abbreviations: AAS, averaged artifact subtraction; BCG, ballistocardiogram; BOLD, blood oxygen level dependent; DC, direct current; EEG, electroencephalography; FMRI, functional magnetic resonance imaging; HFB, high-frequency burst; IAC, imaging-artifact correction; PCA, principal component analysis; RMS, root mean square; ROC, receiver-operator characteristic; SEP, somatosensory evoked potential; SNR, signal-to-noise ratio; STD, standard deviation.

* Corresponding author. Berlin NeuroImaging Center and Department of Neurology, Charité Universitaetsmedizin, Charitéplatz 1, 10117 Berlin, Germany. Fax: +49 30 450 560 952.
E-mail address: frank.freyer@gmail.com (F. Freyer).

1053-8119/$ – see front matter © 2009 Elsevier Inc. All rights reserved.
doi:10.1016/j.neuroimage.2009.06.022

Bonmassar et al., 1999; Comi et al., 2005). Despite the technical challenges that complicate particularly the assessment of high-frequency EEG acquired during fMRI, cortical rhythms up to 50 Hz related to speech processing (Giraud et al., 2007) and to fMRI resting state networks (Mantini et al., 2007b) have already been successfully investigated. However, also EEG oscillations at higher frequencies are known to be of physiological relevance. For example, attention and memory processing involve frequencies up to 150 Hz (for detailed reviews see Jensen and Colgin, 2007; Jensen et al., 2007). Additionally, high-frequency bursts (HFBs) at around 600 Hz found in human EEG recordings during somatosensory stimulation (Curio, 2000, 2005; Hashimoto, 2000) have been shown to reflect spiking activity in primary somatosensory cortex (Baker et al., 2003). With amplitudes in the nanovolt-range and durations of a few milliseconds, they are among the most subtle physiological signals measurable with EEG. We have previously been able to record HFBs in an interleaved EEG–fMRI setup (Ritter et al., 2008b), i.e. HFBs were acquired from non MR-acquisition ('non-scan') periods between subsequent MR-acquisition ('scan') periods. Using this approach, we showed that amplitude modulations of different HFB components temporally separated by milliseconds were associated with anatomically characteristic and distinct blood oxygen level dependent (BOLD) signal changes along the thalamocortical pathway. The limitation of HFB analysis to non-scan periods, however, is an obvious drawback, reducing fMRI signal-to-noise ratio (SNR) and design flexibility, i.e. the continuous monitoring of HFBs with simultaneous EEG–fMRI is desirable. Continuous assessment of EEG signatures above 100 Hz (in the following referred to as ultrafast/ultrahigh-frequency band) however, is particularly difficult since imaging artifacts mainly due to gradient switching predominantly contaminate this spectral range. In a phantom study it has been recently shown for the first time that imaging artifacts can be successfully removed up to 150 Hz using an advanced EEG–fMRI setup (Mandelkow et al., 2006). However, physiological ultrahigh-frequency EEG signals in the range of 600 Hz have not yet been recovered from fMRI acquisition periods.

The purpose of this study was twofold:

(1) The recovery of ultrahigh-frequency EEG signatures during fMRI acquisition by introducing a new imaging-artifact correction (IAC) approach.
(2) The demonstration of applicability of this approach to the EEG spectrum below the ultrahigh-frequency range.

Purpose (1) was achieved by the following steps:

(a) For data recording, we minimize sampling-based variations of the imaging-artifact waveform, in order to fulfill the prerequisite for optimal IAC based on averaged artifact subtraction (AAS, Allen et al., 2000).
(b) To cope with remaining variations based on other sources we optimize our IAC algorithm.
(c) We evaluate the IAC performance in the ultrahigh-frequency range by comparing HFB features, their corresponding sources, SNR characteristics as well as unaveraged spectra between MR-acquisition and non-acquisition periods given all systematic differences between these two conditions are attributable to imaging-artifact residuals.

Purpose (2) was achieved by a corresponding evaluation of EEG features below the ultrahigh-frequency range.

In addition to the imaging artifact which is related to gradient switching, EEG simultaneously acquired with fMRI is also contaminated by the ballistocardiogram (BCG), which is a physiological cardiac-related artifact generated by heart rate associated movements of the electrodes in the static B0 field of the MR scanner (Allen et al., 1998; Bonmassar et al., 2002; Debener et al., 2008). For both our two purposes, the BCG is of no relevance as we will explain later in the paper.

Methods

Subjects

Simultaneous EEG–fMRI was acquired from 10 healthy right-handed subjects (8 female, 21–31 years). All subjects gave written informed consent according to the Declaration of Helsinki prior to investigation. The study was conducted in compliance with the relevant laws and institutional guidelines and approved by the ethics committee of the Charité University Medicine Berlin. During the experiment subjects were lying relaxed in a supine position in the dimly lit bore of the MR scanner. They were instructed to remain awake with open eyes and to pay attention to the stimulus.

Experimental design

Somatosensory evoked potentials (SEPs) were elicited by transcutaneous constant-current electro-stimulation (DS7A, Digitimer, Hertfordshire, England) of the right median nerve using square-wave pulses of 0.2 ms duration and an intensity of 1.5 times above individual motor threshold. Using ERTS software (BeriSoft Cooperation, Frankfurt, Germany) we employed a blocked stimulation-versus-rest design. Stimulus repetition rate was set to 8 Hz. When applying the modified MR sequence (see section fMRI recording parameters) memory limitations on the MR array processor delimited the number of volume acquisitions per recording session. Therefore for each subject two subsequent sessions of 220 volumes were recorded. Each session lasted 15 min and consisted of 22 blocks (25 s duration per block, separated by 15 s rest periods, 200 trials per block), resulting in an overall number of 4400 trials per session.

In order to exclude factors other than the imaging artifact that might influence HFBs acquired in the MR-environment, in five of the ten subjects one session outside the MR scanner was additionally recorded using the same settings.

Synchronization of EEG and fMRI

Synchronizing the clocks of the EEG and fMRI devices prevents variant sampling of the imaging artifacts and therefore considerably improves IAC, particularly in the ultrahigh-frequency range (Anami et al., 2003; Mandelkow et al., 2006; Ritter et al., 2008a). Our IAC approach used here is based on AAS (Allen et al., 2000), where imaging artifacts are removed by subtracting an artifact template, which is estimated by averaging over a number of gradient onset-locked epochs. Hence consistency across imaging-artifact epochs over time is a key prerequisite for successful IAC with AAS. In order to maximize consistency of imaging artifacts through invariant sampling, the internal clocks of the MR scanner and the EEG were synchronized using a frequency divider (DC-5, Physio Tech, Tokyo, Japan), which receives the 4 MHz TTL signal from the MR clock and sends out a 5 kHz signal driving EEG sampling. We assessed the EEG autocorrelation sequence and ensured that there is no periodic-like behavior indicating failure of synchronization (Mandelkow et al., 2006).

EEG recording parameters

EEG recordings were conducted with a 32 channel MR-compatible EEG system (BrainAmp MR Plus, Brain Products, Munich, Germany) and an MR-compatible EEG-cap (Easy cap, FMS, Herrsching-Breitbrunn, Germany), which comprised ring-type sintered silver chloride electrodes with iron-free copper leads. 21 scalp electrodes were arranged according to the International 10-20 System with the

Please cite this article as: Freyer, F., et al., Ultrahigh-frequency EEG during fMRI: Pushing the limits of imaging-artifact correction, NeuroImage (2009), doi:10.1016/j.neuroimage.2009.06.022

reference located at electrode position FCz. In addition, electrooculogram and electrocardiogram were recorded. Impedances of all electrodes were set below 5 kΩ (Easy caps used in this study were not equipped with current limiting resistors in the electrodes) using an abrasive electrolyte gel (Abralyt 2000, FMS, Herrsching-Breitbrunn, Germany). Two amplifier voltage-resolutions were available: 0.5 μV and 0.1 μV. At a resolution of 0.5 μV a recording range of ±16.384 mV is available, capturing both low-amplitude EEG signals and large imaging artifacts. We did not choose the highest available resolution of 0.1 μV since the resulting decreased recording range would lead to extensive saturation of the imaging artifacts at our filter settings. EEG sampling rate was 5 kHz. To reduce the amplitudes of imaging artifacts and prevent saturation, hardware low-pass filters of around 250 Hz are normally applied before digital recording of the EEG, but this prohibits the evaluation of EEG signatures with ultrahigh-frequency spectral features. To allow acquisition of the entire frequency spectrum of the physiological EEG as well as of the imaging artifact we enabled DC recording and set the cut-off frequency of the built-in low-pass hardware filter to 1 kHz instead of 250 Hz. In order to minimize movement-related EEG artifacts, the subject's head was cautiously fixated in the head-coil with a vacuum cushion.

fMRI recording parameters

fMRI recordings were carried out in a 1.5 T MR Vision scanner (Siemens, Erlangen, Germany). We employed a modified T2*-weighted BOLD sensitive echo planar imaging sequence ('stepping stone') which was specifically developed for imaging-artifact minimization during EEG–fMRI acquisition (Anami et al., 2003). For evaluation of the IAC procedure as proposed here, the EEG needs to comprise imaging-artifact free periods that can be used as a baseline condition. Hence we employed an interleaved fMRI protocol. Recording parameters were as follows: repetition time (TR) = 4070 ms, echo time (TE) = 60 ms, acquisition time (TA) = 1650 ms, slices = 18, volumes = 220 per session (two sessions per subject), voxel size = 3.28 × 3.28 × 6.9 mm^3, flip angle = 90°, and matrix = 64 × 64.

EEG analysis

EEG data analysis was carried out using MATLAB v7.0.4 (the Mathworks Inc., Natick, MA, USA). In the following we explain the steps of our IAC approach and its validation.

Imaging-artifact correction

Imaging artifacts were corrected with an in-house-developed algorithm representing a modification of the widely used AAS method (Allen et al., 2000), which was extended to recover ultrahigh-frequency EEG. IAC was performed separately for each subject, session and EEG recording channel, resulting in a total of 420 performed IAC runs, and consisted of the following steps:

Step 1: sampling of imaging artifacts

The 'stepping stone' MR sequence features a low readout-gradient frequency of approximately 500 Hz and long artifact-free interspaces between imaging-artifact peaks (Anami et al., 2003). In combination with synchronization of EEG and fMRI, this enables constant EEG sampling during low imaging-artifact amplitudes using an EEG sampling rate of 1 kHz. However, for the acquisition of HFBs, a sampling rate of 1 kHz is not sufficient, since the resulting Nyquist frequency of 500 Hz is below the frequency of interest at about 600 Hz. Therefore we used the original sampling rate of 5 kHz. Given the high sampling rate and the broadband filter settings used here, the EEG can go into saturation in some cases. This is illustrated in Fig. 1a. Due to EEG–fMRI synchronization and the specific features of the stepping stone sequence saturation occurs periodically and only every fifth or tenth data point. In such cases we linearly interpolated these singular saturated data points (Figs. 1 b–d). Another source of saturation may arise from DC shifts. In such cases, saturation is occurring continuously and interpolation is not applicable, requiring the entire run to be discarded. We estimated the impact of these two factors (5 kHz sampling and DC drifts) on saturation of our data.

Step 2: Segmentation and definition of scan and non-scan periods

Uncorrected data of one EEG channel were segmented into MR epochs of 1 TR length (4070 ms) time-locked to the MR gradient onset. The first 5 epochs were discarded. The resulting $n \times t$ data matrix $\mathbf{U} = [u_{i,j}]_{i=1,\dots,n;\, j=1,\dots,t}$ comprised $n = 215$ epochs of each $t = 20{,}350$ sampling points. For subsequent IAC and evaluation, $\mathbf{U}$ was partitioned into $\mathbf{U}^{\text{scan}} = [u_{i,j}]_{i=1,\dots,n;\, j=1,\dots,\dot{t}}$ and $\mathbf{U}^{\text{non-scan}} = [u_{i,j}]_{i=1,\dots,n;\, j=\ddot{t},\dots,\dddot{t}}$. $\mathbf{U}^{\text{scan}}$ comprised imaging-artifact afflicted periods of MR acquisition (in the following referred to as *scan periods*), whereas $\mathbf{U}^{\text{non-scan}}$ only included imaging-artifact free periods where no MR acquisition occurred (*non-scan periods*). Scan periods ranged from sampling point 1 to sampling point $\dot{t} = 8192$ (1638.4 ms) relative to MR-acquisition onset. Non-scan periods ranged from sampling point $\ddot{t} = 10{,}000$ (2000 ms) to $\dddot{t} = 18{,}191$ (3638.2 ms) relative to MR-acquisition onset. Duration of MR acquisition was 1650 ms, i.e. a gap of 350 ms after MR-acquisition offset was left out to exclude possible post-gradient oscillations. In order to optimize spectral analysis using Fast Fourier Transforms (FFTs) both scan and non-scan periods were defined to have a length of 2^{13} data points.

For later extraction of ultrahigh-frequency EEG signatures, a band-pass filter (400–1000 Hz, 2nd order Butterworth filter, zero phase shift) was applied to $\mathbf{U}$, $\mathbf{U}^{\text{scan}}$, $\mathbf{U}^{\text{non-scan}}$, resulting in filtered matrices $\mathbf{U}^{\text{uf}}$, $\mathbf{U}^{\text{uf scan}}$ and $\mathbf{U}^{\text{uf non-scan}}$, containing only the ultrafast frequency band.

Step 3: weighted template calculation

Each row in $\mathbf{U}$ comprised one uncorrected MR epoch. The following IAC step was performed iteratively on each epoch $\vec{\boldsymbol{u}}_m = [u_{i,j}]_{i=m, j=1,\dots,t} \in \mathbf{U} \,|\, m = 1,\dots,n$.

For each epoch $\vec{\boldsymbol{u}}_m$ we created an imaging-artifact template $\vec{\boldsymbol{a}}_m$. This was done as follows: first we calculated difference epochs $\vec{\boldsymbol{d}}_{l,m} | l = 1,\dots, n$ by subtracting $\vec{\boldsymbol{u}}_m$ from all epochs of the EEG data matrix $\mathbf{U}$:

$$\vec{\boldsymbol{d}}_{l,m} = \left[d_j\right]_{j=1,\dots,t} = \left[u_{i,j}\right]_{i=1;\, j=1,\dots,t} - \vec{\boldsymbol{u}}_m \,|\, l = 1,\dots,n \tag{1}$$

where $[u_{i,j}]_{i=l, j=1,\dots,t}$ are the epochs in the data matrix $\mathbf{U}$, and $\vec{\boldsymbol{u}}_m$ is the MR epoch to be corrected.

For each difference epoch $\vec{\boldsymbol{d}}_{l,m}$ the power spectral density (PSD) in the 400 to 600 Hz range was calculated. This range represents the predominant frequency range of the imaging artifact of the herein used sequence. Hence the PSD in this range provides a measure for the similarity between the imaging artifact in the MR epoch $\vec{\boldsymbol{u}}_m$ and the imaging artifact in epoch $\vec{\boldsymbol{u}}_l$. The template $\vec{\boldsymbol{a}}_m$ is then calculated by the following formula:

$$\vec{\boldsymbol{a}}_m = \frac{1}{k} \frac{\sum_{i=1}^{k} w^i \bar{D}_m(i)}{\sum_{i=1}^{k} w^i}, \tag{2}$$

where w is a weighting factor, which decays exponentially with decreasing similarity, k is the number of epochs used for calculation of the template $\vec{\boldsymbol{a}}_m$, and $\bar{D}_m$ is an epoch set created from the k difference epochs $\vec{\boldsymbol{d}}_{l,m}$, which exhibit the smallest PSD in the 400 to 600 Hz range. In other words, $\bar{D}_m$ comprises the k epochs which are most similar to $\vec{\boldsymbol{u}}_m$, with similarity defined as described above.

While we used a constant number of epochs for calculation of the template ($k = 30$) we tested different values of w (see section

Please cite this article as: Freyer, F., et al., Ultrahigh-frequency EEG during fMRI: Pushing the limits of imaging-artifact correction, NeuroImage (2009), doi:10.1016/j.neuroimage.2009.06.022

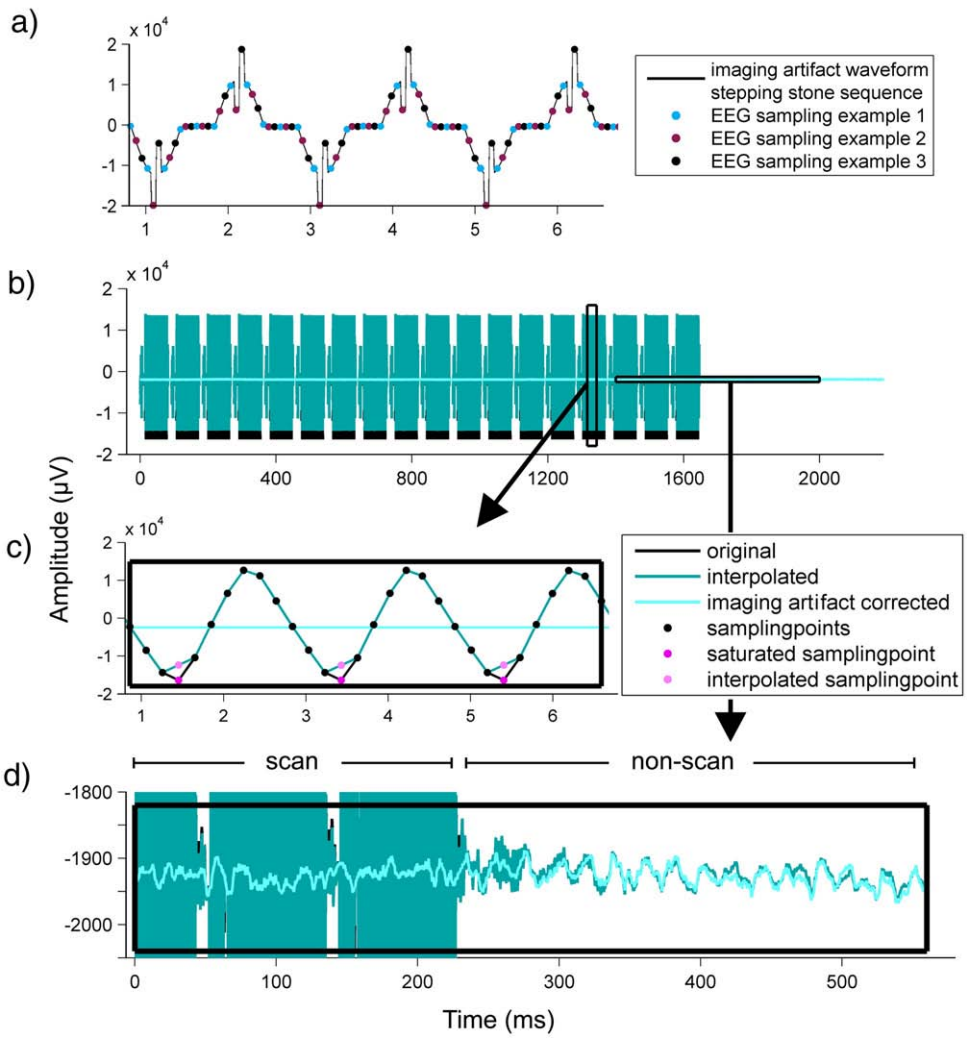

Fig. 1. Interpolation procedure incorporated in our IAC approach. a) Imaging-artifact waveform as induced by the stepping stone sequence (modified from Anami et al., 2003). Colored dots represent different examples of EEG sampling of the imaging artifact. Depending on the particular sampling timing, it is possible that the EEG is saturated periodically at every fifth or tenth data point. b) Example of a scan period plus part of the succeeding non-scan period (single subject EEG data, channel Cp5). Black line: imaging-artifact afflicted original time course; dark cyan line: interpolated time course (identical to original time course apart from every 10th data point); light cyan line: time course after IAC. c) Zoomed-in time window (7 ms) of EEG during a scan period. In this example, every tenth data point (dark pink) is saturated. Prior to IAC we linearly interpolated these data points (light pink). d) In order to also illustrate the underlying physiological EEG (which is visible as a flat line in panel b), we herein show a zoomed-in time window of panel b, comprising part of a scan period plus part of non-scan period before (dark cyan) and after (light cyan) IAC. (For interpretation of the references to colour in this figure legend, the reader is referred to the web version of this article.)

Determination of optimal weighting factors for imaging-artifact template estimation). Our choice of $k=30$ was based on the default settings of the two most frequently used implementations of AAS, namely that of the Brain Vision Analyzer (Brain Products, Munich, Germany) and the EEGLab toolbox (Delorme and Makeig, 2004; Niazy et al., 2005). Note that due to the exponential decay of w, additional epochs do not significantly contribute to template formation (e.g. for $w=0.7$ the 31st epoch in the template would be weighted with $w^{31}=0.7^{31}=0.0000158$).

Epochs during which median nerve stimulation was applied were excluded from template construction in order to avoid contamination of the imaging-artifact template by intermittent stimulation artifacts which can exhibit amplitudes up to 500 µV.

Step 4: averaged artifact subtraction

Finally, the previously calculated imaging-artifact templates were subtracted from the respective epochs:

$$\vec{\boldsymbol{c}}_m = \vec{\boldsymbol{u}}_m - \vec{\boldsymbol{a}}_m | m = 1,\ldots,n, \tag{3}$$

where $\vec{\boldsymbol{u}}_m$ is the artifact-afflicted MR epoch to be corrected and $\vec{\boldsymbol{a}}_m$ is the respective artifact template. All corrected epochs $\vec{\boldsymbol{c}}_m | m=1,\ldots,n$ constitute the data matrix $\mathbf{C} = [c_{i,j}]_{i=1,\ldots,n;\, j=1,\ldots,t}$ which has the same dimensions as $\mathbf{U}$ and is also partitioned into $\mathbf{C}^{\text{scan}} = [c_{i,j}]_{i=1,\ldots,n;\, j=1,\ldots,\dot{t}}$ and $\mathbf{C}^{\text{non-scan}} = [c_{i,j}]_{i=1,\ldots,n;\, j=\ddot{t},\ldots,\ddot{t}}$.

Step 5: broadband PCA-based correction of residual imaging artifacts

In order to preserve the whole frequency spectrum up to ultrahigh frequencies, the usual step of digital low-pass filtering as part of the IAC procedure was not applied here. For the removal of residual imaging artifacts, we performed a principal component analysis (PCA) on the data matrix $\mathbf{C}$, comprising the unfiltered segmented EEG after IAC. The resulting principal component scores $\vec{\boldsymbol{p}}_m [p_j]_{j=1,\ldots,t} | m = 1,\ldots,n$ were ordered according to their eigenvalues, i.e. according to explained variance. The first principal component score, which captured most of the variance time-locked across all aligned MR epochs (i.e. the major imaging-artifact component) was removed from $\mathbf{C}$, resulting in the cleaned data matrix $\mathbf{C}'$. For all further analysis of EEG signatures below the ultrahigh-frequency band (i.e. N20 and spectral bands below

400 Hz), C′ and the respective subsets $\mathbf{C}'^{\text{scan}}$ and $\mathbf{C}'^{\text{non-scan}}$ were used.

Step 6: refinement of imaging-artifact correction for ultrafast EEG by band-specific PCA

As to the ultrahigh-frequency band, further separation of imaging-artifact residuals and physiological EEG signals were necessary. To this end $\mathbf{C}'$ was filtered with a band-pass of 400–1000 Hz, resulting in $\mathbf{C}'^{\text{uf}}$, which contained only ultrafast frequencies. A second, band-specific PCA was then applied to $\mathbf{C}'^{\text{uf}}$, resulting in the principal component score matrix $\mathbf{P}^{\text{uf}} = \left[p_{i,j}^{\text{uf}}\right]_{i=1,\dots,n;\, j=1,\dots,t}$. Also $\mathbf{P}^{\text{uf}}$ is partitioned into subsets $\mathbf{P}^{\text{uf scan}} = \left[p_{i,j}^{\text{uf}}\right]_{i=1,\dots,n;\, j=1,\dots,\dot{t}}$ and $\mathbf{P}^{\text{uf non-scan}} = \left[p_{i,j}^{\text{uf}}\right]_{i=1,\dots,n;\, j=\ddot{t},\dots,\dddot{t}}$ containing scan and non-scan periods. The amount of ultrafast residual imaging artifacts in each principal component score was calculated as follows:

$$\begin{aligned}
\vec{\boldsymbol{r}} &= [\boldsymbol{r}_i]_{i=1,\dots,n} \\
\boldsymbol{r}_i &= \frac{\boldsymbol{q}_i^{\text{scan}}}{\boldsymbol{q}_i^{\text{non-scan}}} \,|\, i = 1,\dots,n \\
\vec{\boldsymbol{q}}^{\text{scan}} &= \left[\boldsymbol{q}_i^{\text{scan}}\right]_{i=1,\dots,n} = \text{RMS}\left(\mathbf{P}^{\text{uf scan}}\right) = \sqrt{\frac{1}{\dot{t}}\sum_{l=1}^{\dot{t}}\left[p_{i,l}^{\text{uf}}\right]^2} \,|\, i = 1,\dots,n \\
\vec{\boldsymbol{q}}^{\text{non-scan}} &= \left[\boldsymbol{q}_i^{\text{non-scan}}\right]_{i=1,\dots,n} = \text{RMS}\left(\mathbf{P}^{\text{uf non-scan}}\right) \\
&= \sqrt{\frac{1}{\dot{t}}\sum_{l=\ddot{t}}^{\dddot{t}}\left[p_{i,l}^{\text{uf}}\right]^2} \,|\, i = 1,\dots,n,
\end{aligned} \tag{4}$$

where vectors $\vec{\boldsymbol{q}}^{\text{scan}}$ and $\vec{\boldsymbol{q}}^{\text{non-scan}}$ are obtained by calculating the root-mean-square (RMS) of the rows of $\mathbf{P}^{\text{uf scan}}$ and $\mathbf{P}^{\text{uf scan}}$, and vector $\vec{\boldsymbol{r}}$ contains the elementwise ratios of $\vec{\boldsymbol{q}}^{\text{scan}}$ and $\vec{\boldsymbol{q}}^{\text{non-scan}} \cdot \boldsymbol{r}_i$ hence indexes the amount of contamination of the *i*th principal component score (i.e. the *i*th row of $\mathbf{P}^{\text{uf}}$) by residual ultrahigh-frequency imaging artifacts. For all *i* with $\boldsymbol{r}_i \geq 2$, the *i*th principal component score was removed from $\mathbf{C}'^{\text{uf}}$, resulting in $\mathbf{C}''^{\text{uf}}$. By removing all scores with corresponding $\boldsymbol{r}_i$ of two or higher, our approach adapts to the (possibly varying) number of scores representing residual imaging artifacts. We favored this approach over removing a fixed number of principal component scores. The value of two represents a compromise between the removal of residual imaging artifacts and biosignal deterioration. Since the PCA was applied to the MR-locked EEG epochs, removing of principal component scores mainly eliminates signal variance time-locked to the gradient onset, i.e. residual artifacts; however it is inevitable that also a fraction of physiological EEG activity is removed as well. In order to delimit loss of physiological EEG a maximum of five principal component scores were removed.

For all further analyses of EEG signatures in the ultrahigh-frequency band between 400 and 1000 Hz (i.e. HFBs, and spectral bands above 400 Hz), $\mathbf{C}''^{\text{uf}}$ and the respective subsets $\mathbf{C}''^{\text{uf scan}}$ and $\mathbf{C}''^{\text{uf non-scan}}$ were used.

Evaluation of imaging-artifact correction

Our IAC evaluation is based on the comparison of scan periods to non-scan periods, which act as an imaging-artifact free reference. In comparison to EEG obtained outside the scanner, non-scan periods from inside the scanner are a better suited (and the best available) reference since differences can mainly be ascribed to the imaging artifact (Ritter et al., 2007). Here we evaluated quality of low and ultrahigh-frequency somatosensory evoked EEG activity by means of the primary cortical component N20 and HFBs, respectively. Additionally, we evaluated spectral EEG characteristics up to 1 kHz. Ten different EEG signals of interest (mean amplitude of the N20, mean RMS amplitude of the HFBs, and mean FFT-spectra of eight defined frequency bands) were compared between three conditions: uncorrected during non-scan periods (in the following referred to as *non-scan-corrected*), imaging-artifact corrected during scan periods (*scan-corrected*), and imaging-artifact corrected during non-scan periods (*non-scan-corrected*). For the evaluation of IAC, three ratios were obtained:

$$R^{\text{IAR}} = \frac{cEEG^{\text{scan}}}{cEEG^{\text{non-scan}}}, \tag{5}$$

where $cEEG^{\text{non-scan}}$ represents the value of one the ten EEG signatures of interest at a time, calculated for artifact condition *non-scan-corrected*, and $cEEG^{\text{scan}}$ represents the value of the same EEG signature during artifact condition *scan-corrected*. Details on the calculation of individual signatures (mean amplitude of the N20, mean RMS amplitude of the HFBs, and mean FFT-spectra of eight defined frequency bands) are described in the respective sections Evaluation of IAC for slow and ultrafast SEP components (N20 and HFBs) and Spectral content of EEG below. R^{IAR} reflects the degree of imaging-artifact reduction and is hence referred to in the following as 'imaging-artifact reduction'. This is not equivalent to 'IAC' which refers to the imaging-artifact correction algorithm.

$$R^{\text{BSD}} = \frac{cEEG^{\text{non-scan}}}{uEEG^{\text{non-scan}}}, \tag{6}$$

where $cEEG^{\text{non-scan}}$ is the same as in Eq. (5) and $uEEG^{\text{non-scan}}$ represents the value of the same EEG signature during artifact condition *non-scan-uncorrected*. R^{BSD} reflects the deterioration of the physiological EEG signal (further termed 'biosignal deterioration').

$$R^{\text{IAC}} = \frac{cEEG^{\text{scan}}}{uEEG^{\text{non-scan}}}, \tag{7}$$

where $cEEG^{\text{scan}}$ are $uEEG^{\text{non-scan}}$ the same as in Eqs. (5) and (6). R^{IAC} aggregates the effects of imaging-artifact reduction and biosignal deterioration by reflecting differences between artifact-corrected periods and the original uncorrected EEG during non-scan periods. The three ratios R^{IAR}, R^{BSD}, and R^{IAC} were calculated for each of the ten EEG signatures of interest.

Determination of optimal weighting factors for imaging-artifact template estimation

Since the parameter *w* for weighting MR epochs used for template calculation has an impact on the outcome of the IAC, we tested 6 different values (0.5, 0.6, 0.7, 0.8, 0.9, and 1.0) for *w* in order to determine which value provides optimal IAC. For each value of *w* we assessed biosignal deterioration and imaging-artifact reduction by calculating the respective ratios R^{BSD} and R^{IAR} (see section Evaluation of imaging-artifact correction). Since improved imaging-artifact reduction can be associated with increased biosignal deterioration and vice versa, a receiver-operator characteristic (ROC) approach was applied in order to find the optimal trade-off between the two measures. Mean spectral amplitudes in eight defined frequency bands were calculated (see section Spectral content of EEG). Then ratios of mean spectral amplitudes between artifact conditions were obtained (see section Evaluation of imaging-artifact correction). For each of the eight frequency bands, absolute deviations of the respective ratio R^{IAR} from one were calculated for the six tested weighting factors *w* in each subject and channel, indicating imaging-artifact reduction. All values were then normalized by subtracting the smallest of all six values. A value of zero hence corresponded to the *w* with the best outcome on imaging-artifact reduction here achieved. After normalization, values were averaged across channels and subjects, yielding six values per frequency band according to the six values of *w*. The same procedure was carried out for the ratio R^{BSD} indicating biosignal deterioration. Finally, values representing biosignal deterioration were plotted against values representing imaging-artifact reduction, yielding

Please cite this article as: Freyer, F., et al., Ultrahigh-frequency EEG during fMRI: Pushing the limits of imaging-artifact correction, NeuroImage (2009), doi:10.1016/j.neuroimage.2009.06.022

Table 1

Variable name	Description	Calculated from data matrix
$uHFB^{\text{non-scan}}$	Mean HFB RMS amplitude of condition *non-scan-uncorrected*	$\mathbf{U}^{\text{uf non-scan}}$
$cHFB'^{\text{non-scan}}$	Mean HFB RMS amplitude of condition *non-scan-corrected*	$\mathbf{C}'^{\text{uf non-scan}}$
$cHFB'^{\text{scan}}$	Mean HFB RMS amplitude of condition *scan-corrected* before 2nd PCA	$\mathbf{C}'^{\text{uf scan}}$
$cHFB'^{\text{all}}$	Mean HFB RMS amplitude of entire dataset before 2nd PCA	$\mathbf{C}'^{\text{uf}}$
$cHFB'^{\text{non-scan}}$	Mean HFB RMS amplitude of condition *non-scan-corrected* after 2nd PCA	$\mathbf{C}'^{\text{uf non-scan}}$
$cHFB'^{\text{scan}}$	Mean HFB RMS amplitude of condition *scan-corrected* after 2nd PCA	$\mathbf{C}'^{\text{uf scan}}$
$cHFB'^{\text{all}}$	Mean HFB RMS amplitude of entire dataset after second band-specific PCA	$\mathbf{C}'^{\text{uf}}$
$uN20^{\text{non-scan}}$	Mean N20 amplitude of condition *non-scan-uncorrected*	$\mathbf{U}^{\text{non-scan}}$
$cN20^{\text{non-scan}}$	Mean N20 amplitude of condition *non-scan-corrected*	$\mathbf{C}'^{\text{non-scan}}$
$cN20^{\text{scan}}$	Mean N20 amplitude of condition *scan-corrected*	$\mathbf{C}'^{\text{scan}}$
$cN20^{\text{all}}$	Mean N20 amplitude of entire dataset	$\mathbf{C}'$

Left column: list of variables representing mean single subject HFB and N20 amplitudes of different 'artifact conditions'.Middle column: descriptions of data contained in each variable. Right column: underlying data matrices of which variables were calculated by re-segmentation aligned to median nerve stimulus onset and averaging.

ROC-like curves. The optimal trade-off between these two measures was determined by selecting the value for w exhibiting the smallest Euclidian distance to the origin.

Evaluation of IAC for slow and ultrafast SEP components (N20 and HFBs)

HFBs were calculated for all subjects and channels and sessions, separately for seven artifact conditions (all artifact conditions are listed in Table 1). For each artifact condition the respective underlying data matrix was re-segmented relative to median nerve stimulus onset and baseline-corrected (baseline was defined as 4–13 ms after stimulation). The same number N of trials was used in all conditions (2020 on average per session, trials of both sessions were concatenated in each subject, trials with amplitudes exceeding 50 μV due to e.g. movement artifacts and surplus trials at the end of the sessions were discarded). For each artifact condition, mean HFB amplitudes were defined as the RMS value in time window 16–25 ms of the respective stimulus-locked epochs averaged across all trials.

For the N20 component, the same procedure was applied, but on different data matrices (see Table 1). For the extraction of the N20 component, we filtered the data matrices with a band-pass of 40–400 Hz. The cut-off frequency of 40 Hz compensates for low-frequency drifts due to e.g. steady state effects of slow late SEP components. N20 amplitudes were defined as the absolute baseline-to-peak amplitude of the first negative peak in the time window 16–25 ms of the respective stimulus-locked epochs averaged across all trials.

Variables representing single subject mean HFB/N20 amplitudes of different artifact conditions and underlying data matrices are listed in Table 1. The second band-specific PCA in the ultrahigh-frequency band did not apply to the low-frequency N20 component and hence in contrast to HFBs the corresponding conditions did not exists for the N20 component. For further evaluation of IAC, HFB/N20 amplitudes of channel Cp5 located over the somatosensory cortex contralateral to stimulation were used and ratios between HFB/N20 amplitudes of the different conditions were calculated (see section Evaluation of imaging-artifact correction).

In addition for each condition HFB and N20 variance was calculated as the standard deviation of the amplitude across trials (further termed $\sigma uHFB^{\text{non-scan}}$, $\sigma uN20^{non\text{-}scan}$, etc.). Single-trial signal-to-noise ratios (SNR_{st}) of HFBs and N20 were calculated for all artifact conditions and for the entire data set after IAC as follows. Since mean amplitudes did not systematically change between conditions (see Results section), we always used $uHFB^{\text{non-scan}}$ and $uN20^{\text{non-scan}}$ as reference signals:

$$SNR_{\text{st}}(X) = \frac{uHFB^{\text{non-scan}}}{\sigma X}\,|X \in \left\{ \begin{array}{l} uHFB^{\text{non-scan}};\text{cHFB}'^{\text{non-scan}};\text{cHFB}'^{\text{scan}};\text{cHFB}'^{\text{all}}; \\ \text{cHFB}''^{\text{non-scan}};\text{cHFB}''^{\text{scan}};\text{cHFB}''^{\text{all}} \end{array} \right\} \tag{8}$$

$$SNR_{\text{st}}(X) = \frac{uN20^{\text{non-scan}}}{\sigma X}\,|X \in \left\{ uN20^{\text{non-scan}};cN20^{\text{non-scan}};cN20^{\text{non-scan}};cN20^{\text{all}} \right\}, \tag{9}$$

SNR of the single subject mean HFBs and N20 amplitude of the individual artifact conditions (in the following referred to as averaged-trials SNR or SNR_{avg}) were determined as follows:

$$SNR_{\text{avg}}(X) = SNR_{\text{st}}(X)\sqrt{N}, \tag{10}$$

where SNR_{st} (X) represents SNR_{st} of HFB/N20 in different artifact conditions as defined in Eqs. (8) and (9), and N is the number of trials. This estimation is motivated by the assumption of normally distributed noise, which decreases with averaging by the square root of the number of trials averaged, leading in turn to an increase of the SNR.

Source reconstruction of HFBs and N20

As an evaluation of the EEG data quality across multiple channels, we performed a dipole source reconstruction of HFBs during all artifact conditions. After alignment to the individual N20 latency (Jones et al., 2000), single subject multichannel HFBs were separately grand averaged for each artifact condition. Subsequently, we conducted source analyses separately for the three grand averages using BESA software (Brain Electrical Source Analysis, MEGIS Software GmbH Munich, Germany). Models of HFB sources comprising three dipoles were computed based on a generic 4-shell spherical head volume conductor model using the recursive multiple signal classification (R-MUSIC) algorithm with sequential brain source imaging (Mosher et al., 1999; Scherg and Von Cramon, 1985). For the resulting dipoles goodness of fit, locations (Talairach coordinates), orientations (xyz-axis), source waveforms and latency of the maximal amplitude were compared between artifact conditions. In addition, for condition *scan-corrected* the source localization was performed after the first broadband and after the second band-specific PCA-based correction of imaging-artifact residuals. For the low-frequency SEPs, a single dipole was fitted at the N20 latency for the grand average of each artifact condition using the same procedure.

Spectral content of EEG

In addition to the high- and low-frequency SEP components, we analyzed the spectral content of the non-task-locked EEG in artifact conditions *non-scan-uncorrected*, *non-scan-corrected* and *scan-corrected*. To this end FFTs (2^{13} data points, resolution 0.6105 Hz) of EEG data matrices $\mathbf{U}^{\text{non-scan}}$, $\mathbf{C}'^{\text{non-scan}}$, and $\mathbf{C}'^{\text{scan}}$ were calculated and averaged across MR epochs, resulting in three averaged spectra per subject and channel. Finally, one grand average per artifact condition was calculated across all channels and subjects. We used the

conventional definitions of frequency bands up to the gamma range. In addition, very fast activity in the ranges of 100 to 250 Hz (Lenz et al., 2008) and 400 to 1000 Hz (Curio, 2005) has been reported. We therefore subdivided the ultrafast band above 100 Hz into three ranges. We hence analyzed spectral amplitudes classified into eight non-overlapping bands: theta (1–4 Hz), delta (4–8 Hz), alpha (8–12 Hz), beta (12–30 Hz), gamma (30–100 Hz), ultrafast-1 (100–250 Hz), ultrafast-2 (250–400 Hz), and ultrafast-3 (400–1000 Hz). For the ultrafast-3 band, spectral amplitudes were specified after the first broadband (i.e. from data matrices $\mathbf{C}'^{\text{uf scan}}$ and $\mathbf{C}'^{\text{uf non-scan}}$) and after the second band-specific PCA-based correction of imaging-artifact residuals (i.e. from data matrices $\mathbf{C}''^{\text{uf scan}}$ and $\mathbf{C}''^{\text{uf scan}}$). In order to avoid contamination of spectral analyses, stimulus artifacts induced by the electrical median nerve stimulation were removed by linear interpolation between −1 and +4 ms around stimulation. Spectral amplitudes in these eight bands of different artifact conditions were used to estimate the ratios for evaluation of IAC (see section Evaluation of imaging-artifact correction).

Interleaved versus continuous EEG–fMRI: signal-to-noise ratio and design flexibility of HFB and N20 measurement protocols

In order to assess possible benefits of continuous acquisition of ultrahigh-frequency EEG during fMRI, we compared SNR characteristics and design flexibility of three different EEG–fMRI scenarios: (*sce*1) an interleaved fMRI protocol with EEG analyzed during imaging-artifact free periods (*sce*2) an interleaved fMRI protocol with EEG analyzed continuously, and (*sce*3) a continuous fMRI protocol with continuous EEG analysis. We compared the scenarios with respect to:

—*SNR of EEG data*: we utilized the previously calculated SNR_{avg} of HFBs in different conditions to determine the SNR_{avg} of the three scenarios.

$$SNR_{\text{avg}}(sce1) = SNR_{\text{avg}}\left(uHFB^{\text{non-scan}}\right), \tag{11}$$

where SNR_{avg} (*sce*1) is the averaged-trials SNR of scenario *sce*1 which equals that of artifact condition *non-scan-uncorrected*.

$$SNR_{\text{avg}}(sce2) = SNR_{\text{avg}}\left(\text{cHFB}''^{\text{all}}\right), \tag{12}$$

where SNR_{avg} (*sce*2) is the averaged-trials SNR of scenario *sce*2 which equals that of the entire imaging-artifact corrected dataset.

$$SNR_{\text{avg}}(sce3) = SNR_{\text{avg}}\left(\text{cHFB}''^{\text{scan}}\right)\sqrt{2} \tag{13}$$

where SNR_{avg} (*sce*13) is the averaged-trials SNR of scenario *sce*3 which was estimated by multiplying the SNR of condition *scan-corrected* with $\sqrt{2}$, assuming normally distributed noise and acquisition of twice the number of trials during the same time. For the N20 component, the calculation was done accordingly.

—*SNR of fMRI data*: since the determination of the exact averaged-trials SNR of fMRI data depends on the protocol and analysis used, we infer the direction of fMRI–SNR change compared to scenario *sce*1.

—*Design flexibility of EEG and of fMRI*: we compared the three scenarios with respect to the restrictions they impose on possible experimental paradigms and scientific questions.

Spectral properties of the ballistocardiogram

The focus of this study was (1) the recovery of ultrahigh-frequency EEG signatures during fMRI acquisition and (2) the demonstration of applicability of our approach to the EEG spectrum below the ultrahigh-frequency range. The BCG had not to be removed for these purposes.

In order to assure that the BCG in our data has no spectral overlap with the ultrahigh-frequency range, we analyzed the averaged time course, event-related spectral perturbation (ERTS) and inter-trial coherence (ITC) of BCG-locked EEG (QRS peak detection via Brain Vision Analyzer software, all other analyses via EEGLab toolbox, Delorme and Makeig, 2004). The channel with the highest BCG amplitude was chosen for analysis.

FMRI analysis

Functional MRI data were analyzed with SPM5 (www.fil.ion.ucl.ac.uk/spm). The first five scans were discarded to avoid spin-saturation effects. Preprocessing included realignment, normalization to the MNI standard brain, spatial smoothing (5 mm smoothing kernel), and temporal high-pass filtering (128 s). In order to assess fMRI correlates of somatosensory stimulation, a conventional model containing a blockwise stimulation-versus-rest function convolved with the HRF, its first and second derivatives and six sets of realignment parameters were estimated.

Results

Synchronization of EEG and fMRI

We assessed the EEG autocorrelation sequence in all subjects, sessions and channels in order to look for periodic-like behavior indicating failure of synchronization (Mandelkow et al., 2006). In all subjects, sessions and channels, EEG autocorrelation did not exhibit a periodic-like behavior thus indicating that synchronization of EEG and fMRI was successful in all cases.

EEG analysis

Sampling of imaging artifacts

Linear interpolation of every fifth or tenth data point was performed in 51 of all 420 IAC runs (10 subjects, 2 sessions, 21 channels), where periodic saturation occurred. In total, the percentage of interpolated data points was 1.93%. Continuous saturation due to strong DC drifts was found in 9 of the 420 IAC runs. These runs were discarded.

Processing time

We assessed the processing time of our modified AAS-procedure. For one subject and one session of 15 min, IAC of 21 EEG channels took 9 min and 38 s on a standard computer (2.6 GHz AMD Opteron Dual Core Processor, 4 GB RAM). Although the processing time depends on various factors, such as EEG sampling rate, number of volumes or the total acquisition time, our exemplary results indicate that our proposed method can be used for off-line IAC in a reasonable amount of time.

Determination of optimal weighting factors for imaging-artifact template estimation

In our proposed IAC procedure, we employed a weighting factor reflecting MR epoch similarity for template calculation. This modification increases concordance between imaging-artifact template and individual imaging-artifact waveform.

The effects of the six tested values of *w* on the non-task-locked EEG after IAC are illustrated in Fig. 2. Two main effects can be recognized. First, with decreasing *w* spectral peaks, reflecting the amount of residual artifacts, decreased. Reducing *w* had a positive effect on the imaging-artifact reduction, since MR epochs less identical to the epoch to be corrected will have a weaker influence on the template. For large values of *w*, these less identical epochs have more impact on the shape

Please cite this article as: Freyer, F., et al., Ultrahigh-frequency EEG during fMRI: Pushing the limits of imaging-artifact correction, NeuroImage (2009), doi:10.1016/j.neuroimage.2009.06.022

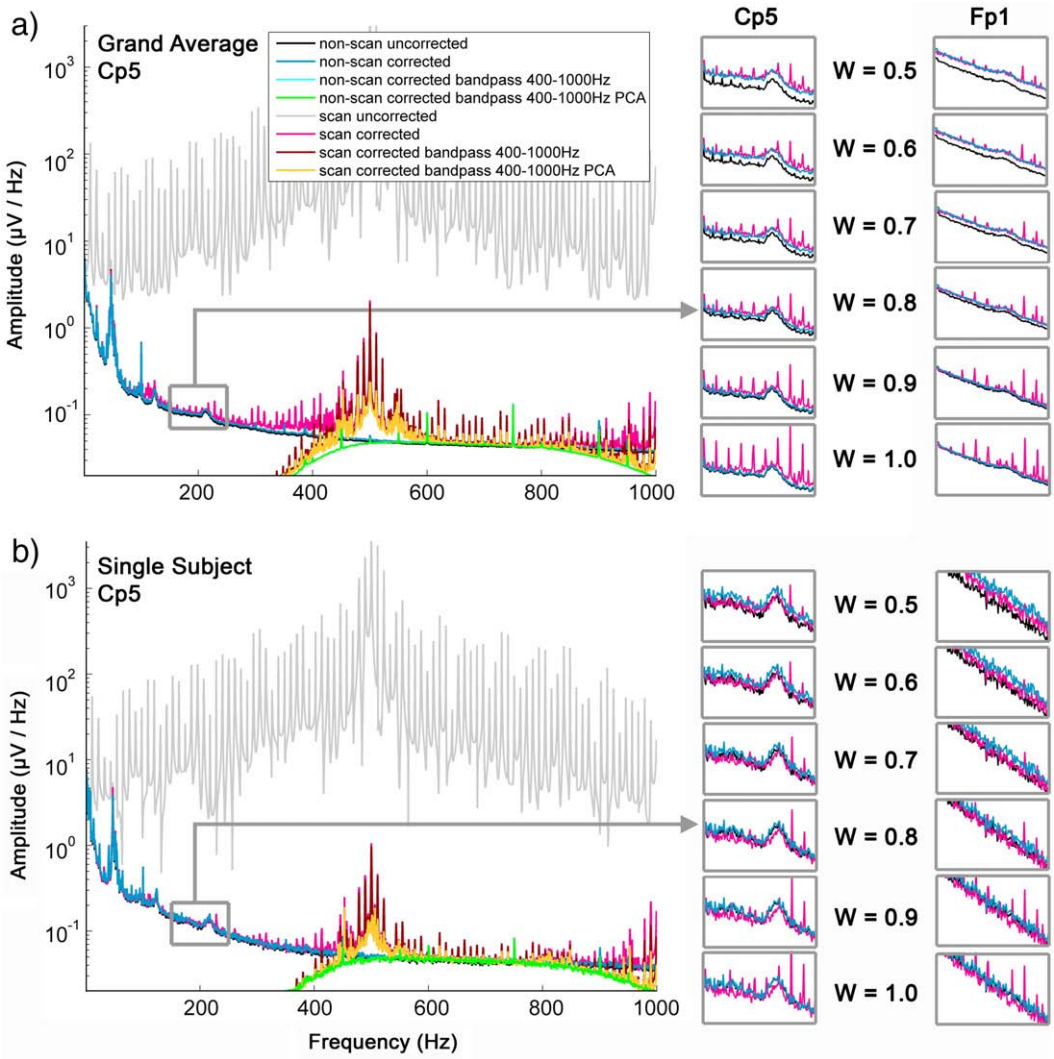

Fig. 2. FFT spectra (1–1000 Hz, channel Cp5) of a) grand averaged and b) single subject EEG. Depicted are 8 partly overlapping spectra of the 4 steps of the IAC procedure: 1. → uncorrected → 2. broadband-corrected → 3. broadband-corrected and band-pass filtered (400–1000 Hz) → 4. broadband-corrected, band-pass filtered (400–1000 Hz) and band-specific PCA-based corrected), both for scan and non-scan periods. Boxes on the right show the zoomed-in frequency range 150–250 Hz for channels Cp5 and Fp1, illustrating the effect of different weighting factors *w* on imaging-artifact reduction and biosignal deterioration.

of the template and hence when subtracting the template, more residual imaging artifacts remain.

Second, with decreasing *w* the broadband power increases after IAC. A quantitative illustration of the impact of IAC with different *w* on biosignal preservation in individual frequency bands is provided in Supplementary Fig. 1. It can be seen that across subjects, sessions and channels, the spectral power increases significantly in each frequency band with decreasing *w*. It seems that with decreasing *w* the physiological EEG is averaged out to a lesser degree during template calculation. When subtracting such contaminated templates from the respective MR epochs to be corrected, the additionally introduced variance leads to a broadband spectral amplitude increase as seen in Fig. 2. Thus, when reducing *w*, biosignal deterioration increases. The observed spectral amplitude increases are proportional to the corresponding spectral EEG amplitudes, further supporting the theory that residual physiological EEG causes this phenomenon. In conclusion, reducing *w* increases biosignal deterioration.

In order to find the optimal trade-off between the two above described converse effects of the weighting factor *w* on biosignal deterioration and imaging-artifact reduction, we applied an ROC-like approach (Fig. 3). Table 2 lists optimal weighting factors of *w* for each frequency band.

Refinement of imaging-artifact correction for ultrafast EEG by band-specific PCA

After the broadband IAC including the first PCA, remaining residual ultrahigh-frequency imaging artifacts were further attenuated by applying the second band-specific PCA (Table 2, Figs. 2 and 4). The effects of the second band-specific PCA are described in more detail in the following sections.

Evaluation of IAC for slow and ultrafast SEP components (N20 and HFBs)

Mean amplitudes, RMS values, latencies, corresponding individual STD, and resulting single-trial and averaged-trials SNR of HFBs and N20 components for each artifact condition as well as the resulting ratios between conditions are listed in Table 2. Fig. 5 shows the grand average HFBs and N20 components of the three artifact conditions. Our results indicate that N20 components and HFB averages are consistent between artifact conditions in terms of latency and waveform (see Fig. 5 and Table 2). Statistical testing (Student's *t*-test) yielded no significant differences in average HFB RMS amplitudes between conditions (*scan-corrected* versus *non-scan-corrected*: $p = 0.58$, *non-scan-uncorrected* versus *non-scan-corrected*: $p = 0.96$, *scan-corrected* versus *non-scan-uncorrected*: $p = 0.55$). With respect to HFBs recovered during scan periods, the second band-

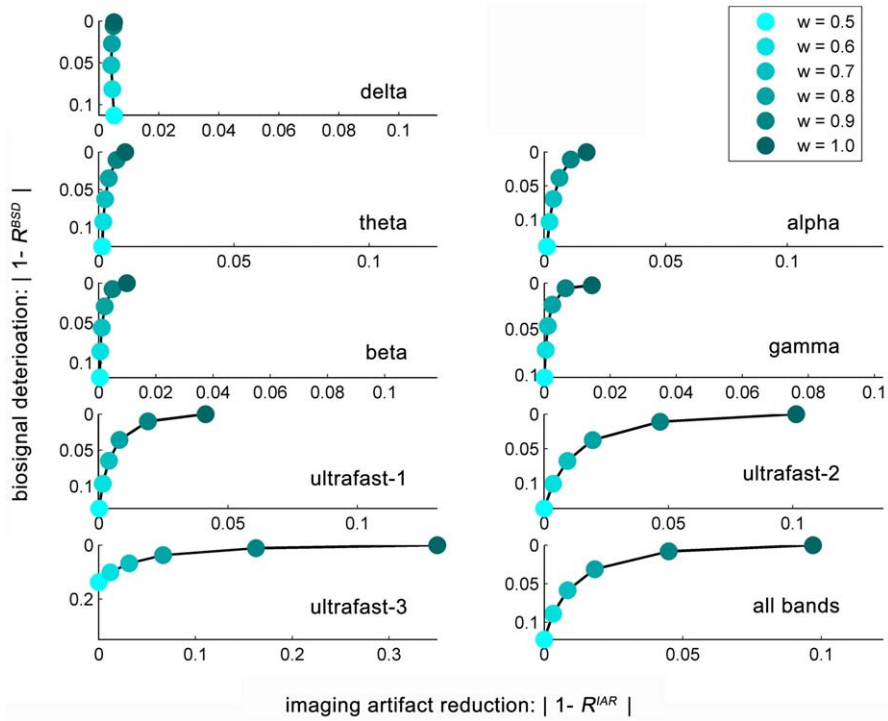

Fig. 3. ROC-like curves were used for the determination of the weighting factor yielding the optimal trade-off between imaging-artifact reduction (*x*-axis) and biosignal deterioration (*y*-axis). Plotted are absolute deviations of ratios from one for the six tested weighting factors, averaged over all electrodes and subjects. Before averaging, all values are normalized by subtracting the smallest of all six values. A value of zero hence indicates the *w* with the best outcome on imaging-artifact reduction or biosignal deterioration herein achieved. The optimal value of *w* was determined by finding the point on the curve with the least Euclidian distance to the origin (top left).

specific PCA-based removal of imaging-artifact residuals reduced the within-subject STD of 231% down to 139% in relation to the STD of non-artifact-afflicted HFBs.

In order to exclude factors other than the imaging artifact that might influence HFBs acquired in the MR-environment, we additionally acquired HFBs outside the MR scanner in five of the ten subjects. As shown in Supplementary Fig. 2, average HFB waveforms are almost identical and RMS amplitude of HFB averages as well as within-subject STD across trials do not vary significantly (Wilcoxon signed rank test, $p = 0.185$ and $p = 0.3125$, respectively)

Table 2
Three artifact conditions and respective ratios (see section Evaluation of imaging-artifact correction).

	$uEEG^{\text{non-scan}}$	$cEEG^{\text{non-scan}}$	$cEEG^{\text{scan}}$	$R^{\text{IAR}} = \frac{cEEG^{\text{scan}}}{cEEG^{\text{non-scan}}}$	$R^{\text{BSD}} = \frac{cEEG^{\text{non-scan}}}{uEEG^{\text{nonscan}}}$	$R^{\text{IAC}} = \frac{cEEG^{\text{scan}}}{uEEG^{\text{non-scan}}}$	w
	Mean (STD)			Mean/mean (STD/STD)			
a)							
HFB RMS amplitude before 2nd PCA	0.134 (1.011) μV	0.133 (1.068) μV	0.129 (2.332) μV	96 (218)%	99 (106)%	96 (231)%	0.8
HFB RMS amplitude after 2nd PCA	0.134 (1.011) μV	0.130 (1.060) μV	0.123 (1.412) μV	94 (133)%	97 (105)%	92 (139)%	0.8[1]
HFB latency	19.22 ms	19.24 ms	19.23 ms	100%	100%	100%	–
N20 amplitude	2.317 (4.602) μV	2.294 (4.612) μV	2.324 (4.940) μV	101(107)%	99 (100)%	100 (107)%	1.0
b)							
HFB SNR_{st} before 2nd PCA	0.131	0.126	0.058	46%	95%	44%	0.8
HFB SNR_{st} after 2nd PCA	0.131	0.125	0.094	75%	96%	72%	0.8[1]
HFB SNR_{avg} before 2nd PCA	5.862	5.614	2.572	46%	95%	44%	0.8
HFB SNR_{avg} after 2nd PCA	5.862	5.606	4.210	75%	96%	72%	0.8[1]
N20 SNR_{st}	0.347	0.349	0.334	96%	101%	96%	1.0
N20 SNR_{avg}	15.503	15.595	14.938	96%	101%	96%	1.0
c)							
Delta (1–4 Hz)	3.570 (2.058) μV	3.503 (1.900) μV	3.498 (1.832) μV	100 (96)%	98 (92)%	98 (89)%	1.0
Theta (4–7 Hz)	2.359 (1.259) μV	2.369 (1.214) μV	2.388 (1.200) μV	101 (99)%	100 (96)%	101 (95)%	1.0
Alpha (8–12 Hz)	1.613 (0.989) μV	1.646 (0.952) μV	1.624 (0.909) μV	99 (95)%	102 (96)%	101 (92)%	0.9
Beta (13–30 Hz)	0.769 (0.421) μV	0.775 (0.418) μV	0.780 (0.414) μV	101 (99)%	101 (99)%	101 (98)%	0.9
Gamma (30–100 Hz)	0.418 (0.214) μV	0.419 (0.222) μV	0.420 (0.215) μV	100 (97)%	100 (104)%	101 (100)%	0.9
Ultrafast-1 (100–250 Hz)	0.120 (0.106) μV	0.124 (0.105) μV	0.130 (0.100) μV	105 (95)%	103 (99)%	108 (94)%	0.9
Ultrafast-2 (250–400 Hz)	0.069 (0.057) μV	0.073 (0.057) μV	0.081 (0.058) μV	110 (102)%	106 (100)%	116 (103)%	0.8
Ultrafast-3 (400–1000 Hz) before 2nd PCA	0.040 (0.024) μV	0.042 (0.025) μV	0.062 (0.039) μV	147 (157)%	105 (103)%	155 (162)%	0.8
Ultrafast-3 (400–1000 Hz) after 2nd PCA	0.040 (0.024) μV	0.042 (0.024) μV	0.052 (0.029) μV	123 (120)%	104 (101)%	128 (121)%	0.8[1]

a) Mean RMS values/latencies of HFBs and amplitudes of N20 components of channel Cp5 averaged across subjects; b) single-trial and averaged-trials SNR of HFBs and N20 of channel Cp5 averaged across subjects; c) FFT amplitudes (moduli of the Fourier transform) for eight frequency bands, averaged across all channels and subjects. In brackets: individual STD averaged across subjects, indicating the mean intra-subject variability. The rightmost column lists optimal weighting factors.

[1] Weighting factor was inherited from ultrafast band/HFBs before 2nd PCA.

Please cite this article as: Freyer, F., et al., Ultrahigh-frequency EEG during fMRI: Pushing the limits of imaging-artifact correction, NeuroImage (2009), doi:10.1016/j.neuroimage.2009.06.022

ARTICLE IN PRESS

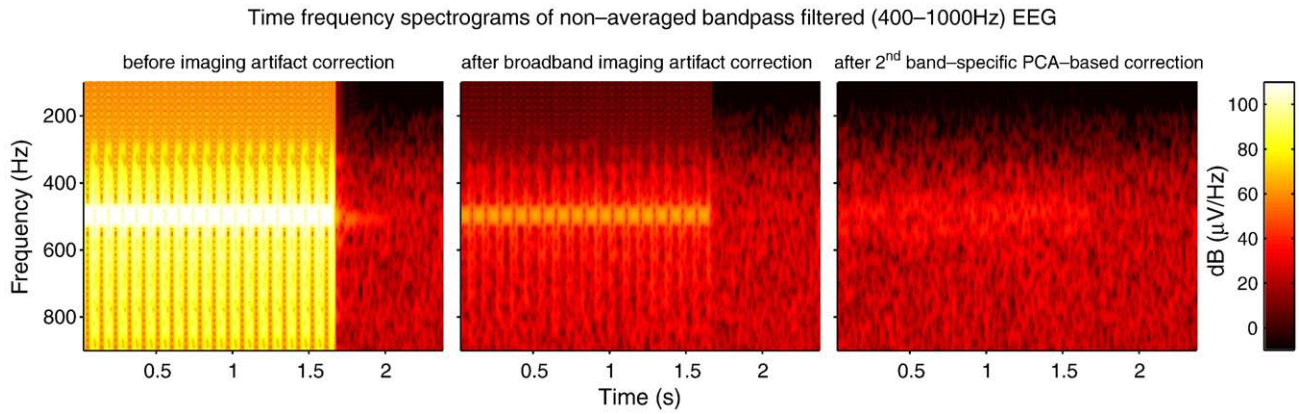

Fig. 4. Effect of band-specific PCA on imaging-artifact residuals. Depicted are three unaveraged EEG time-frequency spectrograms during scan acquisition after band-pass filtering with 400 to 1000 Hz (single subject, channel Cp5) at different degrees of IAC.

for EEG data acquired outside the scanner and EEG of condition *non-scan-uncorrected*, indicating that the imaging artifact is the almost exclusive source of extra variance in the MR-environment. For the N20 component, although the average signal is consistent inside and outside the scanner (see Supplementary Fig. 2), within-subject STD increases inside the scanner, most likely caused by the BCG. Thus for the recovery of low-frequency signals such as the N20 component BCG correction is required. For the evaluation of IAC, however, scan and non-scan periods (both obtained inside the scanner) are compared and for this purpose no BCG correction is necessary.

Source reconstruction of HFBs and N20

For all artifact conditions the three-dipole model fit of the HFBs resulted in one deep subcortical source located close to the thalamus contralateral to stimulation which reflected an early HFB component, as well as two cortical sources, which were located close to the somatosensory cortex contralateral to stimulation and reflected late HFB components. Talairach coordinates and orientations of dipoles are listed in Table 3. For the artifact conditions *non-scan-corrected* and *scan-corrected*, source waveforms and dipole locations are depicted in Fig. 6. Condition *non-scan-uncorrected* closely corresponds to condition *non-scan-corrected* and therefore is not depicted. All three models reached an overall goodness of fit above 95%. Notably, dipole fitting for the *scan-corrected* condition prior to the second PCA-based correction failed to produce reasonable sources, indicating again that removal of residual imaging artifacts by band-specific PCA considerably improves data quality.

For the N20 component, the single dipole fit reached an overall goodness of fit above 99% in all conditions and resulted in identical orientation and nearly identical location for all three conditions (Table 3).

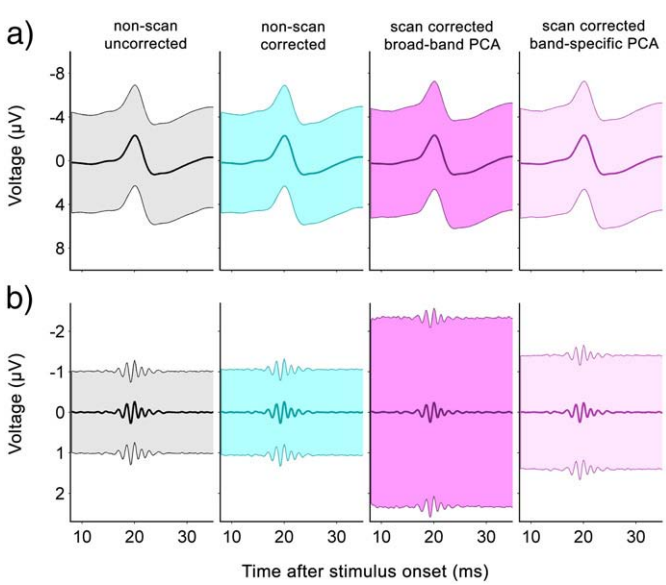

Fig. 5. Grand averaged SEPs for different artifact conditions. For condition *scan-corrected*, SEPs are depicted after broadband and after band-specific PCA-based removal of imaging-artifact residuals. Highlighted colored areas show grand averaged within-subject STDs across trials, indicating mean intra-subject variability; a) band-pass filtered (40–400 Hz) SEP with the primary cortical response N20; b) band-pass filtered (400–1000 Hz) SEP revealing superimposed HFBs. Note that scales at the *y*-axis in a) and b) are different. (For interpretation of the references to colour in this figure legend, the reader is referred to the web version of this article.)

Spectral content of EEG

Table 2 lists mean values and STDs of the specified spectral EEG bands for all three artifact conditions. Additionally, the three respective ratios between artifact conditions are listed. Up to 100 Hz all ratios are close to 100%, indicating minimal biosignal deterioration and optimal imaging-artifact reduction. In the range of 100 to 400 Hz deviations between artifact conditions do not exceed 16%. With regard to the ultrafast-3 band (400–1000 Hz) which is most susceptible to imaging-artifact residuals, deviations amount to less than 28% after the second PCA-based removal of imaging-artifact residuals. Fig. 2 shows broadband FFT spectra of all three conditions and the effect of the second PCA-based correction, both in a single subject and for grand averaged data.

Interleaved versus continuous EEG–fMRI: signal-to-noise ratio and design flexibility of HFB and N20 measurement protocols

The results of comparing three scenarios (1: interleaved fMRI/interleaved EEG; 2: interleaved fMRI/continuous EEG; 3: continuous fMRI/continuous EEG) were the following (see also Table 4):

—*SNR of EEG data*: the estimated SNR_{avg} of HFBs and N20 for each scenario are listed in Table 4. Considering a purely interleaved protocol as baseline condition (scenario *sce*1), adding scan periods to EEG data analysis (scenario *sce*2) would yield an HFB/N20 SNR_{avg} increase of 15%/39%. A purely continuous protocol (scenario *sce*3) also leads to a slight increase in HFB SNR_{avg} of 2%, despite the lower SNR_{st}, which is due to the doubling of available trials compared to an interleaved EEG analysis. For the N20 a continuous protocol (scenario *sce*3) would yield an increase of 36%.

Please cite this article as: Freyer, F., et al., Ultrahigh-frequency EEG during fMRI: Pushing the limits of imaging-artifact correction, NeuroImage (2009), doi:10.1016/j.neuroimage.2009.06.022

Table 3
Spatiotemporal source reconstruction of HFBs and N20.

	Non-scan uncorrected	Non-scan corrected	Scan corrected
a) HFBs (band-pass 400–1000 Hz)			
Talairach coordinates			
D1	[−27.1 −19.8 +11.1]	[−28.0 −18.7 +10.3]	[−25.4 −16.0 +22.7]
D2	[−41.1 −15.5 +36.6]	[−41.5 −15.2 +36.7]	[−45.0 −14.8 +43.4]
D3	[−47.6 −31.3 +35.0]	[−39.3 −18.3 +50.0]	[−49.8 −36.8 +28.5]
Orientation [*x y z*]			
D1	[+0.3 +0.5 −0.8]	[+0.3 +0.5 −0.8]	[+0.3 +0.4 −0.9]
D2	[−0.2 −0.8 −0.6]	[−0.2 −0.8 −0.6]	[−0.2 −0.8 −0.5]
D3	[−0.4 +0.3 +0.9]	[−0.7 −0.6 +0.2]	[−0.2 +0.4 +0.9]
Goodness of fit	97.8%	97.5%	95.1%
b) N20 (band-pass 40–400 Hz)			
Talairach coordinates			
D1	[−40.7 −18.0 +42.1]	[−40.7 −18.0 +42.1]	[−40.7 −15.9 +40.5]
Orientation [*x y z*]			
D1	[+0.4 +0.9 +0.2]	[+0.4 +0.9 +0.2]	[+0.4 +0.9 +0.2]
Goodness of fit	99.8%	99.8%	99.8%

Talairach coordinates and orientations of dipoles as well as the overall goodness of fit of the source model are listed for each artifact condition.

—*SNR of fMRI data*: considering scenario *sce*1 as reference, averaged-trials SNR of fMRI data does not change for scenario *sce*2, since the same fMRI protocol is used. For scenario *sce*3, averaged-trials SNR increases since more volumes can be acquired during the same period of time.

—*Design flexibility of EEG and of fMRI*: in scenarios *sce*2 and *sce*3 continuous EEG can be utilized, in contrast to scenario *sce*1, which increases design flexibility. In scenario *sce*2, imaging-artifact corrected periods exhibit similar noise levels as imaging-artifact free periods for the N20 component enabling high design flexibility, while for HFBs, scenario *sce*2 yields alternating periods of lower and higher noise levels which may constrain limits to the design flexibility. For scenario *sce*3, however, this is not the case since the noise level is constant over the entire EEG for both N20 and HFBs. As for EEG data, continuous acquisition of fMRI (scenario *sce*3) may increase flexibility in comparison to an interleaved acquisition (scenarios *sce*1 and *sce*2).

Spectral properties of the ballistocardiogram

In Supplementary Fig. 3 we show that while the ERSP and inter-trial coherence ITC of the BCG is high at frequencies up to 25 Hz, neither ERSP nor ITC exhibit significant deviations from baseline in the ultrahigh-frequency band between 400 and 1000 Hz. In contrast, HFBs show significant ERSP and ITC changes between 400 and 1000 Hz, as expected. Hence we have shown that the BCG is of no significance and can be ignored when recovering ultrahigh frequencies (our purpose 1). This is of course not the case for the recovery of low-frequency EEG signals that have a spectral overlap with the BCG. In this study, however, we were interested whether our IAC approach is appropriate for low-frequency EEG signals and did not intend to recover the true underlying neuronal low-frequency signal. For the evaluation of IAC quality as done here (i.e. by comparing MR-acquisition and non-

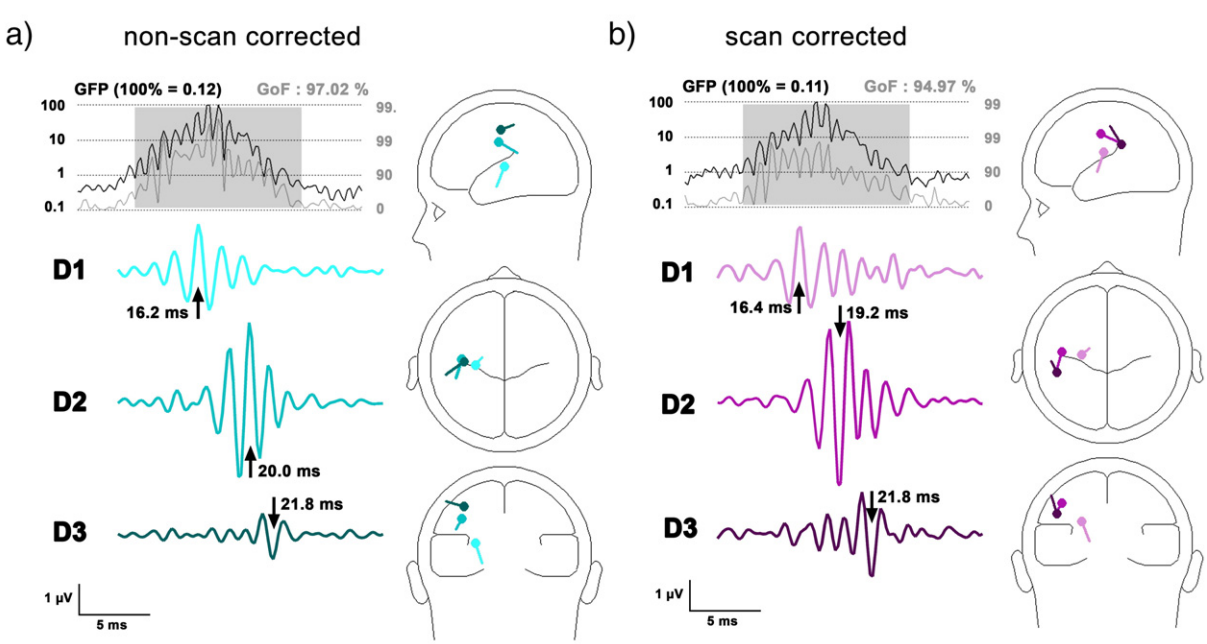

Fig. 6. Dipole source reconstruction of HFBs separately obtained from a) non-scan and b) scan periods after IAC. For both artifact conditions, source reconstruction resulted in one subcortical source located close to the thalamus contralateral to stimulation reflecting an early HFB component, as well as two cortical sources located close to the somatosensory cortex contralateral to stimulation reflecting late HFB components. Talairach coordinates and orientations of dipoles are listed in Table 3. GFP: global field power, GoF: goodness of fit.

Please cite this article as: Freyer, F., et al., Ultrahigh-frequency EEG during fMRI: Pushing the limits of imaging-artifact correction, NeuroImage (2009), doi:10.1016/j.neuroimage.2009.06.022

Table 4
Schematic illustration of the three possible EEG–fMRI scenarios and relevant experimental parameters.

	Scenario *sce1* (reference) fMRI interleaved EEG interleaved	Scenario *sce2* fMRI interleaved EEG continuous	Scenario *sce3* fMRI continuous EEG continuous
SNR_{avg} (HFBs)	5.86	6.72	5.95
	↔	↑ (+15%)	↔ (+2%)
SNR_{avg} (N20)	15.50	21.56	21.13
	↔	↑ (+39%)	↑ (+36%)
SNR fMRI	↔	↔	↑
Flexibility EEG	↔	↑	↑
Flexibility fMRI	↔	↔	↑

Scenario *sce*1 represents the baseline condition, arrows in scenarios *sce*2 and *sce*3 indicate increase or decrease of the respective experimental parameter in comparison to scenario *sce*1. For averaged-trials SNR of HFBs and N20 percent changes are indicated in parentheses.

acquisition periods), the BCG is of no relevance and needs not to be removed.

FMRI analysis

Although the evaluation of EEG data quality was the main focus of this study, we also analyzed the acquired fMRI data. Fig. 7 provides an example of a single subject result, showing a highly significant positive BOLD response in the somatosensory cortex contralateral to stimulation.

Discussion

We have shown that (1) recovery of ultrafast EEG signatures from fMRI acquisition periods is feasible with our optimized EEG–fMRI setup and IAC algorithm and (2) this IAC approach is also valid for the EEG spectrum below the ultrahigh-frequency range. Point 1 was achieved by the following steps:

(1a) Optimization of acquisition setup: we used a DC to 1 kHz hardware filter to capture both physiological ultrahigh-frequency EEG and undistorted imaging artifacts, we synchronized the EEG and fMRI devices in order to minimize variations of the imaging-artifact waveform due to variant sampling, and we employed the stepping stone sequence which was specifically developed for imaging-artifact minimization.

(1b) Optimization of imaging-artifact algorithm: we improved our IAC algorithm in order to cope with imaging-artifact variations independent of sampling. This improved algorithm comprises a new type of template calculation, including a similarity measure for imaging artifacts and optimized exponential weighting according to similarity. We further refined removal of ultrahigh-frequency residuals by a cascade of broadband and band-specific PCA.

(1c) Evaluation of the IAC performance in the ultrahigh-frequency range: we validated the recovery of ultrahigh-frequency EEG signatures by assessing HFB features, their corresponding sources and SNR characteristics as well as unaveraged EEG spectra.

Point 2 was achieved by:

(2) Evaluation of the IAC performance below the ultrahigh-frequency range: corresponding to point (1c) we performed an evaluation of EEG features below the ultrahigh-frequency range.

In the following we discuss the above described individual steps, the legitimation of our evaluation approach, and some general considerations concerning EEG–fMRI.

Optimization of acquisition setup (1a)

By employing a particular combination of acquisition settings comprising a broadband DC to 1 kHz hardware filter, synchronization of EEG and fMRI and the artifact-minimizing stepping stone sequence, we met the requirements for recovery of ultrahigh-frequency EEG signals during imaging-artifact periods. With this filter configuration, a standard MRI sequence leads to frequent and en-bloc saturation of the EEG since high-frequency components of imaging artifacts are less attenuated. This renders recovery of the EEG by interpolation impossible. In contrast the stepping stone sequence allows invariant and low-amplitude sampling of imaging artifacts (Fig. 1) and saturation occurs in rare cases limited to singular data points that can be interpolated. Thus, we fulfilled the requirements for further optimal processing of imaging artifacts. In future experiments, the utilization of a stepping stone sequence optimized for 5 kHz sub-sampling is desirable. However, we show that even the original stepping stone sequence developed by Anami et al. (2003) for 1 kHz sub-sampling is sufficient to fully recover HFBs during MR-acquisition periods.

Optimization of imaging-artifact algorithm (1b)

Despite careful exclusion of imaging-artifact variations caused by inconsistent sampling, imaging artifacts still exhibit other sources of

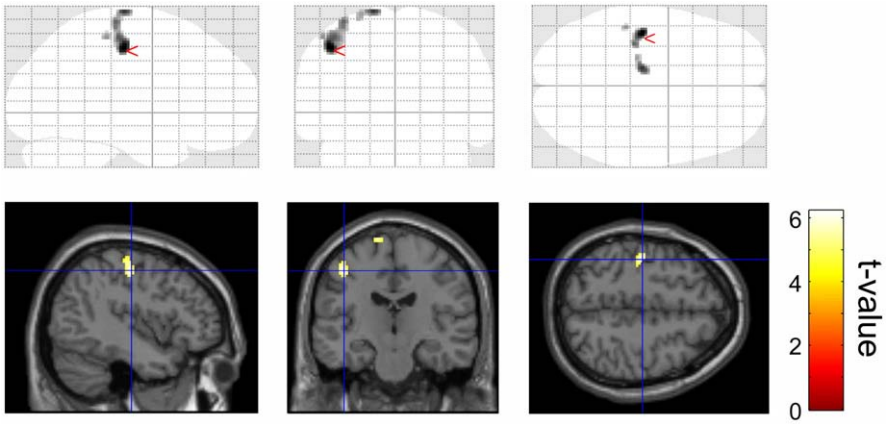

Fig. 7. FMRI correlates of blockwise electrical median nerve stimulation in an exemplary single subject. Statistical parametric maps (SPMs) show a single highly significant activation cluster in the primary somatosensory cortex contralateral to stimulation. The *t*-value at the peak voxel (red arrow, MNI coordinates [−42, −18, 50]) is 6.2, corresponding to $p<0.0005$, False-Discovery-Rate (FDR) corrected for multiple comparisons. Top row: sagittal, coronal and axial views of glassbrain SPMs. Bottom row: SPMs superimposed on the T1-weighted anatomical reference image. SPMs were thresholded at a *t*-value of 4.305, corresponding to $p<0.01$, FDR-corrected. (For interpretation of the references to colour in this figure legend, the reader is referred to the web version of this article.)

Please cite this article as: Freyer, F., et al., Ultrahigh-frequency EEG during fMRI: Pushing the limits of imaging-artifact correction, NeuroImage (2009), doi:10.1016/j.neuroimage.2009.06.022

variations due to movement-induced changes in position or orientation of EEG electrodes in relation to the magnetic field or due to variations of the magnetic field gradients. The former can be caused by slow or fast subject movements or scanner vibrations, the latter by thermal noise drifts of the scanner. Our IAC procedure adapts to such variations of the imaging-artifact waveform. The idea of the template subtraction method is that an artifact epoch **A** is corrected by subtracting a template which consists of an average of other artifact epochs. Any difference between the imaging-artifact waveform in **A** and the template-epoch will result in imperfect IAC. In our approach, templates are generated for each MR epoch by including a constant number of epochs most similar to **A**. These epochs are weighted with an exponential decay depending on similarity. The weighting factor w ensures an over-proportional weighting of similar imaging-artifact epochs and reduces the impact of less similar MR epochs on the template which has a positive effect on imaging-artifact reduction. We applied the exponentially weighted IAC approach with favorable results in previous studies (Becker et al., 2005; Ritter et al., 2007). One goal of this study was to evaluate the frequency-specific impact of different weighting factors on imaging-artifact reduction and biosignal preservation. In order to compare an exponential weighting to a conventional approach without any weighting, we also included the condition of $w = 1$, which reflects the case of no exponential decay. While assessing different weighting factors, we found that improved imaging-artifact reduction is associated with increased biosignal deterioration and vice versa (Figs. 2 and 3). Small weighting factors reduce the impact of less similar MR epochs on the template which has a positive effect on imaging-artifact reduction. However, at the same time smaller weighting factors increase biosignal deterioration, since the imaging-artifact template includes more residual physiological signal not cancelled out introducing additional noise into corrected epochs. We conclude from our results that weighting factors smaller than 0.8 are not beneficial in any frequency band, since the improved imaging-artifact reduction does not compensate for the biosignal deterioration. After application of AAS, residual imaging artifacts still persist in the corrected EEG. Several efforts to reduce these residuals have been made. Allen et al. suggested adaptive noise cancellation as post-processing procedure after AAS and reported efficient correction of artifact residuals for frequencies up to 24 Hz (Allen et al., 2000). Niazy et al. complemented this approach with PCA-based optimal basis sets that reflected variations of imaging artifacts. They were able to sufficiently reduce artifact residuals with frequency components up to 35 Hz (Niazy et al., 2005). Also independent component analysis has been demonstrated to successfully extract and reduce imaging-artifact residuals after AAS, when applied to EEG signals filtered between 0.5 and 40 Hz (Mantini et al., 2007a). In another study, a beamformer spatial filter was used to eliminate residual imaging artifacts from the EEG signal of interest which in that case was a 20 Hz surrogate signal and a visually-evoked physiological oscillatory 17.2 Hz signal (Brookes et al., 2008). All these approaches included low-pass filtering for the reduction of high-frequency imaging-artifact residuals. Since here we focused on the recovery of ultrafast EEG oscillations, low-pass filtering was not applicable. Gradient switching-induced artifacts, however, affect particularly the EEG in the ultrahigh-frequency band (Fig. 2). Therefore, we specifically aimed at reducing ultrahigh-frequency imaging-artifact residuals while preserving the physiological EEG in this band. To this end, we refined our algorithm with a cascaded PCA-based removal of imaging-artifact residuals. After broadband PCA, a second band-specific PCA selectively attenuated ultrahigh-frequency imaging-artifact residuals.

Evaluation of the IAC performance in the ultrahigh-frequency range (1c)

This beneficial impact of the PCA post-processing is reflected in the time-frequency spectrograms (Fig. 4) and spectra (Fig. 2) of the unaveraged EEG as well as in the STD across trials of HFBs acquired during scan periods (Fig. 5). Additionally, successful recovery of HFBs was demonstrated by a spatiotemporal dipole source analysis of HFBs acquired during scan periods, which provided meaningful and expected sources (Curio, 2005; Gobbele et al., 1998; Gobbele et al., 2004; Porcaro et al., 2008; Restuccia et al., 2003) only after band-specific PCA-based correction of imaging-artifact residuals (Fig. 6, Table 3). The advantage of the cascaded PCA is additionally reflected in the spectral amplitudes of the ultrahigh-frequency range which do not exceed 128% of the spectral amplitudes of non-scan periods. Also, the single-trial SNR of HFBs during scan periods reached 72% of the SNR during non-scan periods in contrast to 43% before band-specific PCA. This single-trial SNR level is sufficient to record HFBs continuously during constant fMRI acquisition (scenario *sce*3, Table 4) without a loss of averaged-trials SNR compared to an interleaved EEG–fMRI scenario with HFB analysis of non-scan periods (scenario *sce*1, Table 4). In the case of non-continuous fMRI acquisition and continuous HFB analysis (scenario *sce*2, Table 4), even an averaged-trials SNR of 115% (compared to scenario *sce*1) can be achieved, though HFBs exhibit single-trial SNR differences between scan and non-scan periods. In principle, scenario *sce*3 offers optimal design flexibility and increased fMRI acquisition time. On the other hand, scenario *sce*2 allows ensuring successful IAC (Ritter et al., 2007).

Evaluation of the IAC performance below the ultrahigh-frequency range (2)

Our results do not only indicate good recovery of ultrahigh-frequency signals, but also demonstrate complete recovery of EEG signatures below 100 Hz (spectra and N20 component), amplitudes of which were in the range of 98–102% of that in non-scan periods (Table 2). Hence, although our approach allows for the first time to recover 600 Hz HFBs, it is not restricted to ultrafast frequencies, but can be applied to investigate the entire frequency spectrum of EEG recorded during fMRI. However, when only low-frequency EEG signatures are of interest, the additional band-specific PCA-based post-processing is not required.

Ballistocardiogram artifacts

The BCG is known to have its main spectral components in the low-frequency range between 4 and 8 Hz (Allen et al., 2000) and to have no spectral overlap with the ultrahigh-frequency range as demonstrated in Supplementary Fig. 3. Thus, for the recovery of ultrafast EEG signatures (our purpose 1) the BCG can be neglected.

Also, for the evaluation of IAC in the low-frequency spectrum by comparing MR-acquisition and non-acquisition periods (our purpose 2), the BCG–being present under both conditions–can be ignored (Allen et al., 2000; Anami et al., 2003; Becker et al., 2005; Ritter et al., 2007). However, if the aim is to recover the true underlying neuronal EEG signal in the lower frequency band, this signal most likely has a spectral overlap with the BCG, and the BCG needs to be considered. In this case, our IAC approach can be complemented by one of the various methods available for BCG correction (Allen et al., 1998; Bonmassar et al., 2002; Grouiller et al., 2007; Niazy et al., 2005; Srivastava et al., 2005; Debener et al., 2007; Mantini et al., 2007a,b; Masterton et al., 2007; Brookes et al., 2008; Debener et al., 2008).

FMRI signal quality

FMRI acquisition considerably impairs the EEG signal quality by introducing imaging artifacts into the EEG. Vice versa, EEG acquisition can affect fMRI signal quality as well by introducing susceptibility artifacts to the MRI image. These effects are known to be of low magnitude, particularly when using state-of-the-art EEG equipment (Bonmassar et al., 2001a,b; Goldman et al., 2000; Huang-Hellinger et

Please cite this article as: Freyer, F., et al., Ultrahigh-frequency EEG during fMRI: Pushing the limits of imaging-artifact correction, NeuroImage (2009), doi:10.1016/j.neuroimage.2009.06.022

al., 1995; Ives et al., 1993; Krakow et al., 2000). However, since our method includes also optimized hardware settings including a modified fMRI acquisition sequence ('stepping stone'), we analyzed the acquired fMRI data in order to ensure that fMRI signal quality is satisfying (see Fig. 7).

Conclusion

The ultrahigh-frequency EEG above 100 Hz contains valuable information such as high gamma oscillations involved in attention and memory or HFBs providing a noninvasive window for the monitoring of human population spike activity. The integration of ultrahigh-frequency EEG recordings and fMRI provides new possibilities to explore the mechanisms underlying these ultrafast oscillations. The herein proposed setup renders the reconstruction of broadband EEG up to ultrahigh frequencies during fMRI acquisition periods feasible. It thus enables the uninterrupted spatiotemporal investigation of spontaneous and task-related ultrafast oscillations with simultaneous EEG–fMRI.

Acknowledgments

This work was supported by the German Federal Ministry of Education and Research BMBF (Berlin NeuroImaging Center; Bernstein Center for Computational Neuroscience), the German Research Foundation DFG (Berlin School of Mind and Brain; SFB 618-B4) and the Robert Bosch Foundation.

Appendix A. Supplementary data

Supplementary data associated with this article can be found, in the online version, at doi:10.1016/j.neuroimage.2009.06.022.

References

Allen, P.J., Polizzi, G., Krakow, K., Fish, D.R., Lemieux, L., 1998. Identification of EEG events in the MR scanner: the problem of pulse artifact and a method for its subtraction. NeuroImage 8, 229–239.

Allen, P.J., Josephs, O., Turner, R., 2000. A method for removing imaging artifact from continuous EEG recorded during functional MRI. NeuroImage 12, 230–239.

Anami, K., Mori, T., Tanaka, F., Kawagoe, Y., Okamoto, J., Yarita, M., Ohnishi, T., Yumoto, M., Matsuda, H., Saitoh, O., 2003. Stepping stone sampling for retrieving artifact-free electroencephalogram during functional magnetic resonance imaging. NeuroImage 19, 281–295.

Baker, S.N., Curio, G., Lemon, R.N., 2003. EEG oscillations at 600 Hz are macroscopic markers for cortical spike bursts. J. Physiol. 550, 529–534.

Becker, R., Ritter, P., Moosmann, M., Villringer, A., 2005. Visual evoked potentials recovered from fMRI scan periods. Hum. Brain Mapp. 26, 221–230.

Benar, C.G., Grova, C., Kobayashi, E., Bagshaw, A.P., Aghakhani, Y., Dubeau, F., Gotman, J., 2006. EEG–fMRI of epileptic spikes: concordance with EEG source localization and intracranial EEG. NeuroImage 30, 1161–1170.

Benar, C.G., Schon, D., Grimault, S., Nazarian, B., Burle, B., Roth, M., Badier, J.M., Marquis, P., Liegeois-Chauvel, C., Anton, J.L., 2007. Single-trial analysis of oddball event-related potentials in simultaneous EEG–fMRI. Hum. Brain Mapp. 28, 602–613.

Bonmassar, G., Anami, K., Ives, J., Belliveau, J.W., 1999. Visual evoked potential (VEP) measured by simultaneous 64-channel EEG and 3T fMRI. NeuroReport 10, 1893–1897.

Bonmassar, G., Hadjikhani, N., Ives, J.R., Hinton, D., Belliveau, J.W., 2001a. Influence of EEG electrodes on the BOLD fMRI signal. Hum. Brain Mapp. 14, 108–115.

Bonmassar, G., Schwartz, D.P., Liu, A.K., Kwong, K.K., Dale, A.M., Belliveau, J.W., 2001b. Spatiotemporal brain imaging of visual-evoked activity using interleaved EEG and fMRI recordings. NeuroImage 13, 1035–1043.

Bonmassar, G., Purdon, P.L., Jaaskelainen, I.P., Chiappa, K., Solo, V., Brown, E.N., Belliveau, J.W., 2002. Motion and ballistocardiogram artifact removal for interleaved recording of EEG and EPs during MRI. NeuroImage 16, 1127–1141.

Brookes, M.J., Mullinger, K.J., Stevenson, C.M., Morris, P.G., Bowtell, R., 2008. Simultaneous EEG source localisation and artifact rejection during concurrent fMRI by means of spatial filtering. NeuroImage 40, 1090–1104.

Comi, E., Annovazzi, P., Silva, A.M., Cursi, M., Blasi, V., Cadioli, M., Inuggi, A., Falini, A., Comi, G., Leocani, L., 2005. Visual evoked potentials may be recorded simultaneously with fMRI scanning: a validation study. Hum. Brain Mapp. 24, 291–298.

Curio, G., 2000. Linking 600-Hz "spikelike" EEG/MEG wavelets ("sigma-bursts") to cellular substrates: concepts and caveats. J. Clin. Neurophysiol. 17, 377–396.

Curio, G., 2005. Ultrafast EEG activities. In: Niedermeyer, E., Lopes da Silva, F.H. (Eds.), Electroencephalography. Basic Principles, Clinical Applications, and Related Fields. Lippincott Williams & Wilkins, Philadelphia, pp. 495–504.

Czisch, M., Wehrle, R., Kaufmann, C., Wetter, T.C., Holsboer, F., Pollmacher, T., Auer, D.P., 2004. Functional MRI during sleep: BOLD signal decreases and their electrophysiological correlates. Eur. J. Neurosci. 20, 566–574.

Dang-Vu, T.T., Schabus, M., Desseilles, M., Albouy, G., Boly, M., Darsaud, A., Gais, S., Rauchs, G., Sterpenich, V., Vandewalle, G., Carrier, J., Moonen, G., Balteau, E., Degueldre, C., Luxen, A., Phillips, C., Maquet, P., 2008. Spontaneous neural activity during human slow wave sleep. Proc. Natl. Acad. Sci. U. S. A. 105, 15160–15165.

de Munck, J.C., Goncalves, S.I., Huijboom, L., Kuijer, J.P., Pouwels, P.J., Heethaar, R.M., Lopes da Silva, F.H., 2007. The hemodynamic response of the alpha rhythm: an EEG/fMRI study. NeuroImage 35, 1142–1151.

Delorme, A, Makeig, S, 2004. EEGLAB: an open source toolbox for analysis of single-trial EEG dynamics including independent component analysis. J. Neurosci. Methods 134, 9–21.

Debener, S., Ullsperger, M., Siegel, M., Fiehler, K., von Cramon, D.Y., Engel, A.K., 2005. Trial-by-trial coupling of concurrent electroencephalogram and functional magnetic resonance imaging identifies the dynamics of performance monitoring. J. Neurosci. 25, 11730–11737.

Debener, S, Strobel, A, Sorger, B, Peters, J, Kranczioch, C, Engel, AK, Goebel, R, 2007. Improved quality of auditory event-related potentials recorded simultaneously with 3-T fMRI: removal of the ballistocardiogram artefact. NeuroImage 34, 587–597.

Debener, S., Mullinger, K.J., Niazy, R.K., Bowtell, R.W., 2008. Properties of the ballistocardiogram artefact as revealed by EEG recordings at 1.5, 3 and 7 T static magnetic field strength. Int. J. Psychophysiol. 67, 189–199.

Eichele, T., Specht, K., Moosmann, M., Jongsma, M.L., Quiroga, R.Q., Nordby, H., Hugdahl, K., 2005. Assessing the spatiotemporal evolution of neuronal activation with single-trial event-related potentials and functional MRI. Proc. Natl. Acad. Sci. U. S. A. 102, 17798–17803.

Giraud, A.L., Kleinschmidt, A., Poeppel, D., Lund, T.E., Frackowiak, R.S., Laufs, H., 2007. Endogenous cortical rhythms determine cerebral specialization for speech perception and production. Neuron 56, 1127–1134.

Gobbele, R., Buchner, H., Curio, G., 1998. High-frequency (600 Hz) SEP activities originating in the subcortical and cortical human somatosensory system. Electroencephalogr. Clin. Neurophysiol. 108, 182–189.

Gobbele, R., Waberski, T.D., Simon, H., Peters, E., Klostermann, F., Curio, G., Buchner, H., 2004. Different origins of low- and high-frequency components (600 Hz) of human somatosensory evoked potentials. Clin. Neurophysiol. 115, 927–937.

Goldman, R.I., Stern, J.M., Engel, J., Cohen, M.S., 2000. Acquiring simultaneous EEG and functional MRI. Clin. Neurophysiol. 111, 1974–1980.

Goldman, R.I., Stern, J.M., Engel Jr., J., Cohen, M.S., 2002. Simultaneous EEG and fMRI of the alpha rhythm. NeuroReport 13, 2487–2492.

Goncalves, S.I., de Munck, J.C., Pouwels, P.J., Schoonhoven, R., Kuijer, J.P., Maurits, N.M., Hoogduin, J.M., Van Someren, E.J., Heethaar, R.M., Lopes da Silva, F.H., 2006. Correlating the alpha rhythm to BOLD using simultaneous EEG/fMRI: inter-subject variability. NeuroImage 30, 203–213.

Grouiller, F., Vercueil, L., Krainik, A., Segebarth, C., Kahane, P., David, O., 2007. A comparative study of different artefact removal algorithms for EEG signals acquired during functional MRI. NeuroImage 38, 124–137.

Hamandi, K., Laufs, H., Noth, U., Carmichael, D.W., Duncan, J.S., Lemieux, L., 2008. BOLD and perfusion changes during epileptic generalised spike wave activity. NeuroImage 39, 608–618.

Hashimoto, I., 2000. High-frequency oscillations of somatosensory evoked potentials and fields. J. Clin. Neurophysiol. 17, 309–320.

Huang-Hellinger, F.R., Breiter, H.C., McCormack, G.M., Cohen, M.S., Kwong, K.K., Savoy, R.L., Weisskoff, R.M., Davis, T.L., Baker, J.R., Belliveau, J.W., Rosen, B.R., 1995. Simultaneous functional magnetic resonance imaging and electrophysiological recording. Hum. Brain Mapp. 3, 13–23.

Iannetti, G.D., Niazy, R.K., Wise, R.G., Jezzard, P., Brooks, J.C., Zambreanu, L., Vennart, W., Matthews, P.M., Tracey, I., 2005. Simultaneous recording of laser-evoked brain potentials and continuous, high-field functional magnetic resonance imaging in humans. NeuroImage 28, 708–719.

Ives, J.R., Warach, S., Schmitt, F., Edelman, R.R., Schomer, D.L., 1993. Monitoring the patient's EEG during echo planar MRI. Electroencephalogr. Clin. Neurophysiol. 87, 417–420.

Jensen, O., Colgin, L.L., 2007. Cross-frequency coupling between neuronal oscillations. Trends Cogn. Sci. 11, 267–269.

Jensen, O., Kaiser, J., Lachaux, J.P., 2007. Human gamma-frequency oscillations associated with attention and memory. Trends Neurosci. 30, 317–324.

Jones, M.S., MacDonald, K.D., Choi, B., Dudek, F.E., Barth, D.S., 2000. Intracellular correlates of fast (>200 Hz) electrical oscillations in rat somatosensory cortex. J. Neurophysiol. 84, 1505–1518.

Krakow, K., Allen, P.J., Symms, M.R., Lemieux, L., Josephs, O., Fish, D.R., 2000. EEG recording during fMRI experiments: image quality. Hum. Brain Mapp. 10, 10–15.

Krakow, K., Messina, D., Lemieux, L., Duncan, J.S., Fish, D.R., 2001. Functional MRI activation of individual interictal epileptiform spikes. NeuroImage 13, 502–505.

Laufs, H., Kleinschmidt, A., Beyerle, A., Eger, E., Salek-Haddadi, A., Preibisch, C., Krakow, K., 2003a. EEG-correlated fMRI of human alpha activity. NeuroImage 19, 1463–1476.

Laufs, H., Krakow, K., Sterzer, P., Eger, E., Beyerle, A., Salek-Haddadi, A., Kleinschmidt, A., 2003b. Electroencephalographic signatures of attentional and cognitive default modes in spontaneous brain activity fluctuations at rest. Proc. Natl. Acad. Sci. U. S. A. 100, 11053–11058.

Laufs, H., Daunizeau, J., Carmichael, D.W., Kleinschmidt, A., 2008. Recent advances in recording electrophysiological data simultaneously with magnetic resonance imaging. NeuroImage 40, 515–528.

ARTICLE IN PRESS

Lemieux, L., Krakow, K., Fish, D.R., 2001. Comparison of spike-triggered functional MRI BOLD activation and EEG dipole model localization. NeuroImage 14, 1097–1104.
Lenz, D, Jeschke, M, Schadow, J, Naue, N, Ohl, FW, Herrmann, CS, 2008. Human EEG very high frequency oscillations reflect the number of matches with a template in auditory short-term memory. Brain Res. 1220, 81–92.
Liebenthal, E., Ellingson, M.L., Spanaki, M.V., Prieto, T.E., Ropella, K.M., Binder, J.R., 2003. Simultaneous ERP and fMRI of the auditory cortex in a passive oddball paradigm. NeuroImage 19, 1395–1404.
Mandelkow, H., Halder, P., Boesiger, P., Brandeis, D., 2006. Synchronization facilitates removal of MRI artefacts from concurrent EEG recordings and increases usable bandwidth. NeuroImage 32, 1120–1126.
Mantini, D., Perrucci, M.G., Cugini, S., Ferretti, A., Romani, G.L., Del Gratta, C., 2007a. Complete artifact removal for EEG recorded during continuous fMRI using independent component analysis. NeuroImage 34, 598–607.
Mantini, D., Perrucci, M.G., Del Gratta, C., Romani, G.L., Corbetta, M., 2007b. Electrophysiological signatures of resting state networks in the human brain. Proc. Natl. Acad. Sci. U. S. A. 104, 13170–13175.
Martinez-Montes, E., Valdes-Sosa, P.A., Miwakeichi, F., Goldman, R.I., Cohen, M.S., 2004. Concurrent EEG/fMRI analysis by multiway Partial Least Squares. NeuroImage 22, 1023–1034.
Masterton, RA, Abbott, DF, Fleming, SW, Jackson, GD, 2007. Measurement and reduction of motion and ballistocardiogram artefacts from simultaneous EEG and fMRI recordings. NeuroImage 37, 202–211.
Moosmann, M., Ritter, P., Krastel, I., Brink, A., Thees, S., Blankenburg, F., Taskin, B., Obrig, H., Villringer, A., 2003. Correlates of alpha rhythm in functional magnetic resonance imaging and near infrared spectroscopy. NeuroImage 20, 145–158.
Mosher, J.C., Baillet, S., Leahy, R.M., 1999. EEG source localization and imaging using multiple signal classification approaches. J. Clin. Neurophysiol. 16, 225–238.
Niazy, R.K., Beckmann, C.F., Iannetti, G.D., Brady, J.M., Smith, S.M., 2005. Removal of FMRI environment artifacts from EEG data using optimal basis sets. NeuroImage 28, 720–737.
Porcaro, C., Coppola, G., Di Lorenzo, G., Zappasodi, F., Siracusano, A., Pierelli, F., Rossini, P.M., Tecchio, F., Seri, S., 2008. Hand somatosensory subcortical and cortical sources assessed by functional source separation: an EEG study. Hum. Brain Mapp. 2009, 660–674.
Restuccia, D., Della Marca, G., Valeriani, M., Rubino, M., Paciello, N., Vollono, C., Capuano, A., Tonali, P., 2003. Influence of cholinergic circuitries in generation of high-frequency somatosensory evoked potentials. Clin. Neurophysiol. 114, 1538–1548.
Ritter, P., Villringer, A., 2006. Simultaneous EEG–fMRI. Neurosci. Biobehav. Rev. 30, 823–838.
Ritter, P., Becker, R., Graefe, C., Villringer, A., 2007. Evaluating gradient artifact correction of EEG data acquired simultaneously with fMRI. Magn. Reson. Imaging 25, 923–932.
Ritter, P., Becker, R., Freyer, F., Villringer, A., 2008a. Imaging artefact. In: Mulert, C., L., L. (Eds.), EEG–fMRI Physiology, Technique and Application. Springer.
Ritter, P., Freyer, F., Curio, G., Villringer, A., 2008b. High-frequency (600 Hz) population spikes in human EEG delineate thalamic and cortical fMRI activation sites. NeuroImage 42, 483–490.
Ritter, P., Moosmann, M., Villringer, A., 2008c. Rolandic alpha and beta EEG rhythms' strengths are inversely related to fMRI-BOLD signal in primary somatosensory and motor cortex. Hum. Brain Mapp. 30, 1168–1187.
Salek-Haddadi, A., Merschhemke, M., Lemieux, L., Fish, D.R., 2002. Simultaneous EEG-correlated ictal fMRI. NeuroImage 16, 32–40.
Salek-Haddadi, A., Lemieux, L., Merschhemke, M., Diehl, B., Allen, P.J., Fish, D.R., 2003. EEG quality during simultaneous functional MRI of interictal epileptiform discharges. Magn. Reson. Imaging 21, 1159–1166.
Sammer, G., Blecker, C., Gebhardt, H., Bischoff, M., Stark, R., Morgen, K., Vaitl, D., 2007. Relationship between regional hemodynamic activity and simultaneously recorded EEG-theta associated with mental arithmetic-induced workload. Hum. Brain Mapp. 28, 793–803.
Scheeringa, R., Petersson, K.M., Oostenveld, R., Norris, D.G., Hagoort, P., Bastiaansen, M.C., 2008. Trial-by-trial coupling between EEG and BOLD identifies networks related to alpha and theta EEG power increases during working memory maintenance. NeuroImage 44, 1224–1238.
Scherg, M., Von Cramon, D., 1985. Two bilateral sources of the late AEP as identified by a spatio-temporal dipole model. Electroencephalogr.Clin. Neurophysiol. 62, 32–44.
Schubert, R., Ritter, P., Wustenberg, T., Preuschhof, C., Curio, G., Sommer, W., Villringer, A., 2008. Spatial attention related SEP amplitude modulations covary with BOLD signal in S1—a simultaneous EEG–fMRI study. Cereb. Cortex 18, 2686–2700.
Srivastava, G, Crottaz-Herbette, S, Lau, KM, Glover, GH, Menon, V, 2005. ICA-based procedures for removing ballistocardiogram artifacts from EEG data acquired in the MRI scanner. NeuroImage 24, 50–60.

Please cite this article as: Freyer, F., et al., Ultrahigh-frequency EEG during fMRI: Pushing the limits of imaging-artifact correction, NeuroImage (2009), doi:10.1016/j.neuroimage.2009.06.022